Satellite Spot Ratio Recalibration Report

Robert De Rosa, Vanessa Bailey, Jeffrey Vargas

February 2019

1. Satellite spots – background

Satellite spots are attenuated replicas of the central point spread function generated by placing a periodic grid in the pupil plane of the instrument. These are used to calibrate astrometric and photometric measurements of faint companions to stars observed with GPI. The principles of the technique and the application to high-contrast imaging are described in Sivaramakrishnan & Oppenheimer 2006. The effect of introducing a periodic grid into the pupil plane of GPI is demonstrated using *poppy* in Figure 1.

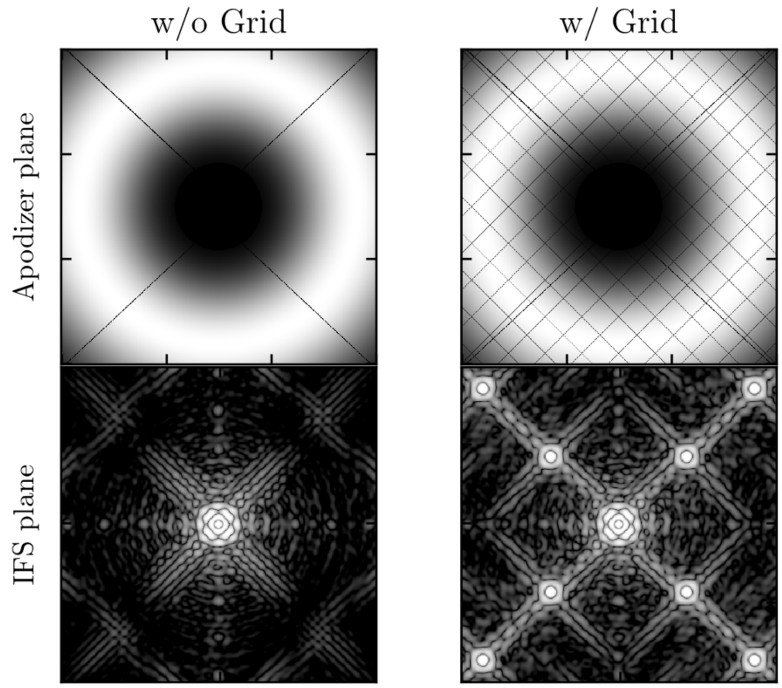

Figure 1: Pupil-plane image at the location of the apodizer (top row) and log-scaled focal-plane image at the IFS (bottom row) with (left column) and without (right column) the grid imprinted on the apodizer. The width of the grid lines sets the flux ratio, and the spacing between the grid lines sets the position in the focal plane.

The separation between the central PSF and the satellite spots is governed by the spacing of the grid lines in the pupil plane, and the ratio of their fluxes is governed by the width of the grid lines. For GPI, the grids imprinted on the apodizer were designed to position the satellite spots at ~20λ/D with a flux ratio of $\sim 2\times10^{-4}$. The same diffractive process also creates higher order spots at integer multiples of the ~20λ/D separation; the second order spots are visible in IFS images at shorter wavelengths (*Y*, *J*). The ratio between these second order spots and the central star was not characterized in the previous analysis.

Additionally, it was not envisaged that the instrument would be used in non-standard configurations where the IFS filter was not matched with the pupil plane apodizer designed for that wavelength. Due to a fault in the pupil plane mechanism, the *H*-band apodizer was used for all observations between mid-2015 and mid-2016, regardless of which IFS filter was selected. It therefore became important to confirm that the satellite spot ratio for the *H*-band apodizer was monochromatic between 1 and 2.5 um.

2. Original Calibration

The original PSF core-to-satellite spot flux ratios (Table 1) used by both the GPI Exoplanet Survey (GPIES) and the wider community were given in Maire et al. 2014. These ratios were measured using data obtained during integration and testing at UC Santa Cruz in 2012, and were validated in *H* band on β Pic and HD 118335 by comparing the measured flux ratio between star and companion to literature measurements, although with significantly larger uncertainties than the laboratory measurements.

Table 1: Satellite spot flux ratios from Maire et al. 2014.

Filter	**Ratio ($\times 10^{-4}$)**	**Δm**
Y	2.34 ± 0.12	9.80 ± 0.05
J	1.80 ± 0.06	9.36 ± 0.03
H	2.04 ± 0.10	9.23 ± 0.06
K1	2.70 ± 0.18	8.92 ± 0.07
K2	1.92 ± 0.46	9.29 ± 0.21

3. Experimental Design

With the exception of the work presented in Section 10, all experiments were performed in the lab using use GPI's internal Artificial Source Unit (ASU).

The $\sim 10^4$ flux ratio between the PSF core and satellite spots prevents a direct measurement of the satellite spot ratio in a single exposure. Instead, a two-step approach is used. Two perpendicular sine wave patterns of equal amplitude are applied to the MEMS deformable mirror (DM) to generate four "DM spots" at a 1:100 flux ratio to the central source, the brightness of the spots being proportional to the square of the amplitude of their respective sine waves. The DM spots' separation is set by the spatial frequency, or "mode number," of the DM sine waves, the clocking by the orientation of the sine waves on the DM. Higher mode numbers correspond to higher spatial frequencies, and thus to more widely separated DM spots. The clocking of the DM spots is chosen such that their diffraction spikes do not overlap the satellite spots.

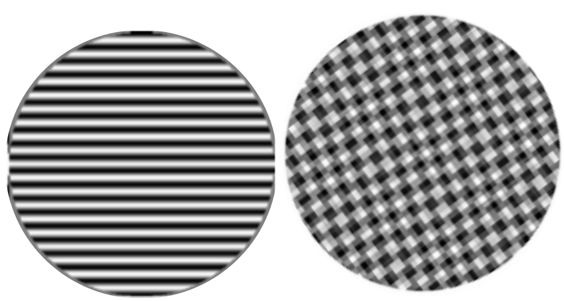

Figure 2: Example DM sinewave patterns. *Left:* a single sinewave produces a pair of spots above and below the PSF core. *Right:* A dual set of sinewaves, clocked at an angle, produces a set of 4 spots similar to those shown in Figure 3.

Images taken with a neutral density (ND) filter are used to measure the flux ratio between the PSF core and the DM spots, and images taken in GPI's coronagraphic mode are used to measure the flux ratio between the DM spots and the satellite spots (Figure 3). These two ratios are multiplied together to calculate the flux ratio of the satellite spots to the PSF core.

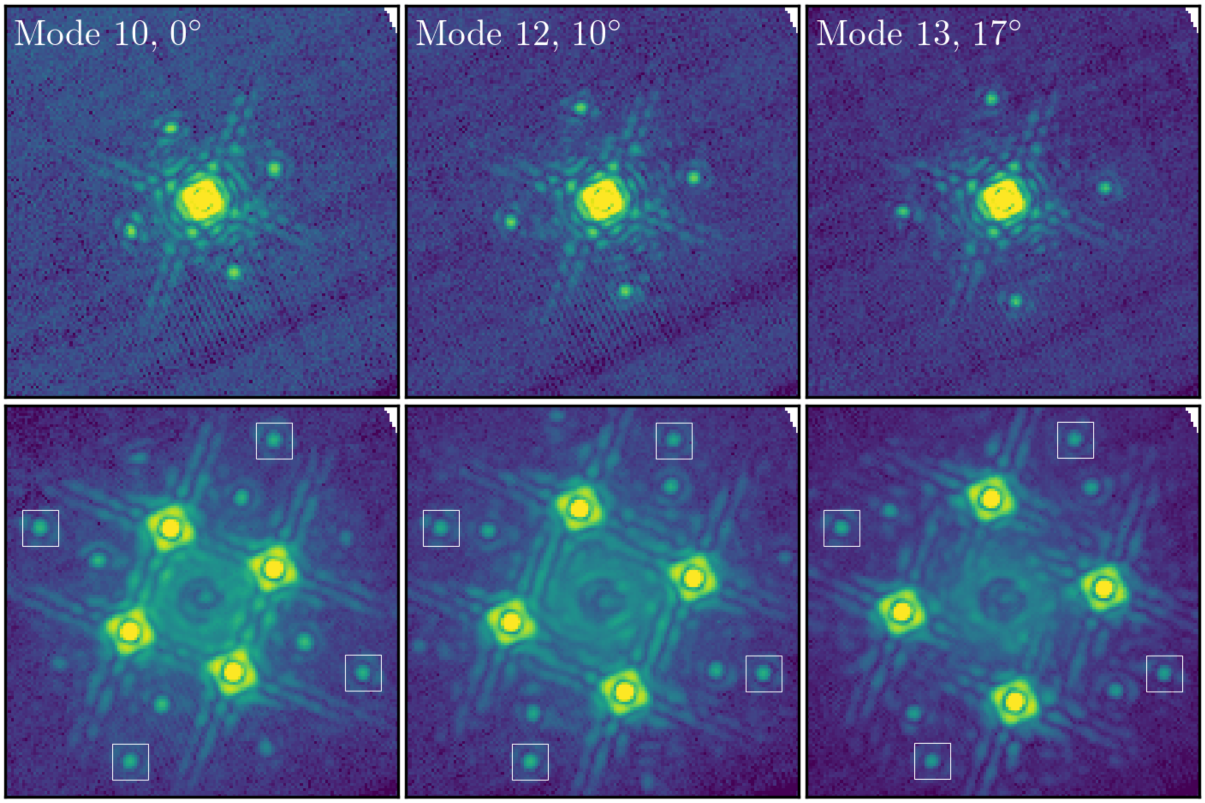

Figure 3: DM spots for three different configurations of the sine wave applied to the tweeter as seen in the ND images (top row) and coronagraphic images (bottom row). The mode corresponds to the spatial frequency of the sine wave (larger mode, higher frequency, spots at a larger separation), and the angle corresponds to the counter-clockwise rotation of the spots in the IFS image. The location of the satellite spots generated by the apodizer grating are highlighted by boxes, not to be confused with the additional sources generate by the bright DM spots.

Table 2 Example instrument configuration for two sets of satellite spot flux ratio measurements, one for the J IFS filter and J apodizer, and one for the same filter but with the H apodizer. FPM = focal plane mask. PPM = pupil plane mask (apodizer or ND).

	J/Japod (ND)	**J/Japod (coron)**	**J/Hapod (ND)**	**J/Hapod (coron)**
Filter	J	J	J	J
FPM	SCIENCE	J	SCIENCE	J
PPM	ND3	J	ND3	H
Lyot	J	J	J	J

A typical sequence consists of at least five images taken with the ND filter, and five in the coronagraphic mode. Exposure times were typically between 1.5 and 6 seconds, coadded to approximately 45 seconds. There are two significant differences between these two imaging modes. 1) Images with the ND filter are taken in *direct* mode (no apodizer[1]) as the ND filter is installed in the same pupil plane mechanism (PPM) as the apodizers, and 2) for the coronagraphic images, the focal plane mechanism (FPM) is changed from SCIENCE (fully reflective) to the occulting spot corresponding to the filter (e.g., FPM_H for *H*-band) and the ND filter is replaced with the apodizer (e.g., APOD_H_G6205 for H-band).

On dates where the satellite spot ratios for multiple apodizers with the same IFS filter were measured (e.g., J filter/J apodizer, J filter/H apodizer), one set of ND images were used for both sets of coronagraphic images as the required instrument configuration was identical (e.g., Table 2). “Background” images (ASU powered off) were obtained for the subset of *K*-band datasets where the instrumental thermal background was at a significant level. Calibration arc and dark frames were taken when necessary.

[1] While the lack of an apodizer in configuration (1) does change the PSF morphology, it does so for both the PSF core and the DM spots. Thus, their flux ratio, the value being measured, is unaffected.

4. Data Reduction and PSF Fitting

Each dataset was reduced in a similar manner with the GPI Data Reduction Pipeline (DRP). The data taken in 2013 were re-reduced with the same DRP version to ensure uniformity. The following primitives were used:

Load Wavelength Calibration
Subtract Dark Background
Destripe Science Image†
Subtract Thermal Sky Background if K Band‡
Update Spot Shifts for Flexure
Interpolate Bad Pixels in 2D Frame
Assemble Spectral Datacube
Interpolate Wavelength Axis
*Interpolate Bad Pixels in Cube**

† For datasets taken in 2013, ‡ For datasets taken in 2013 and 2016, * For H, K1, and K2 datasets

Two primitives were skipped that are typically used for GPIES campaign datasets. *Interpolate Bad Pixels in Cube* was skipped for the shorter wavelengths (Y, J) as this often caused the peaks of the DM spots to be erroneously flagged as bad pixels by the outlier rejection algorithm (although the central pixels themselves were in the linear regime). The *Correct Distortion* was also skipped as it was determined to have a negligible effect on the measured satellite spot ratio. Skipping the final bad pixel correction primitive caused a significant increase in the number of bad pixels in the final data cube. To help mitigate this, a new hot pixel maps was constructed using the 60-second dark sequence obtained on 2016-12-21. This new bad pixel map was used in the reduction of all data obtained in 2016 and 2017.

The locations of the ASU and four DM spots in the ND images, and the location of the four DM spots and four satellite spots (and four second-order spots for Y and J band) in the coronagraphic images, were measured by fitting a two-dimensional symmetric Gaussian to a small 10-pixel stamp extracted at the estimated location with a least-squares optimizer. The full images were high-pass filtered prior to extracting the small stamp to minimize potential biases in fitting faint satellite spots near bright DM spots (Figure 4). The pixel coordinates of the five sources in the ND images, and the eight (or twelve) sources in the coronagraphic images, were saved for each wavelength slice of each image.

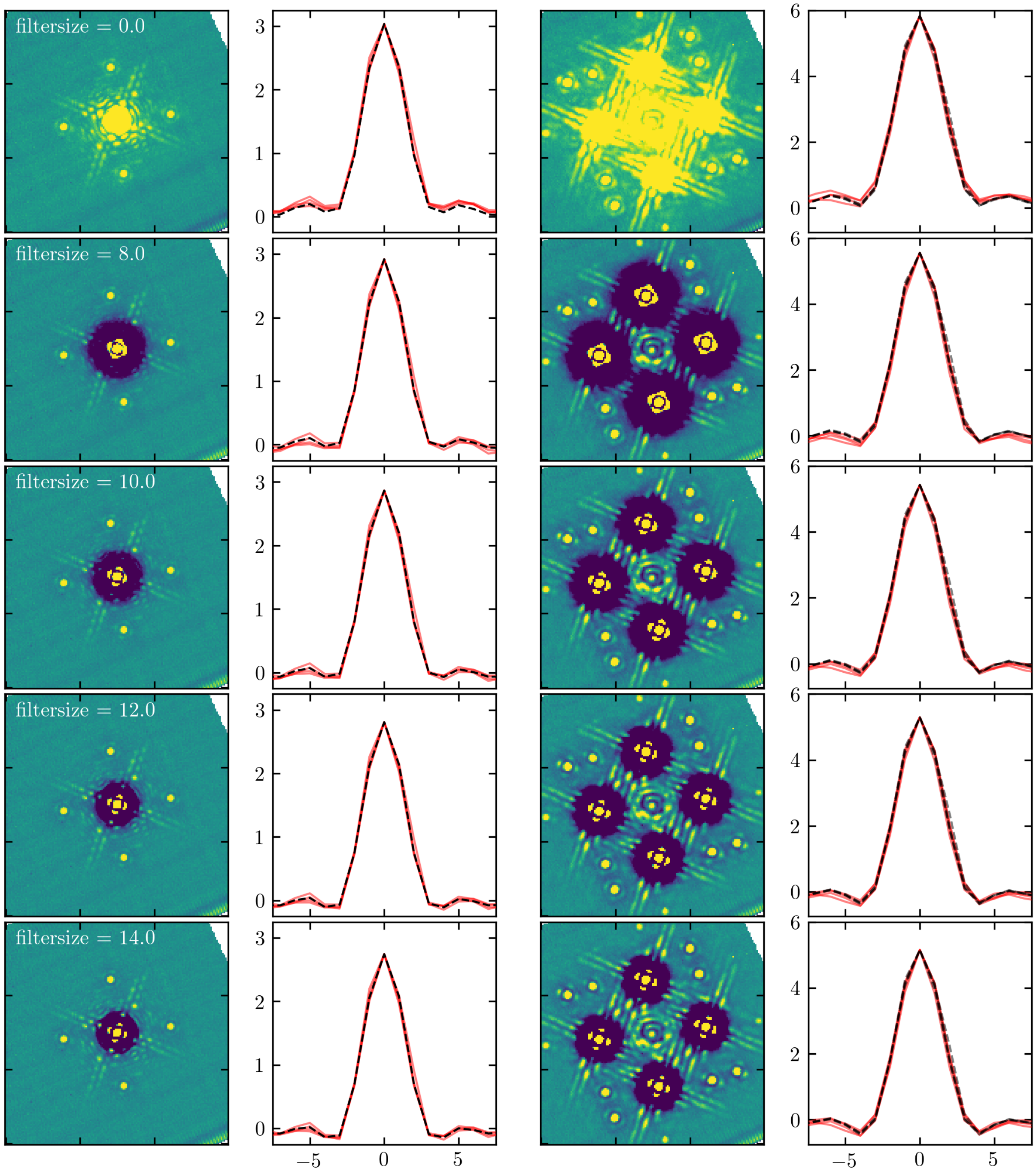

Figure 4: Effect of the Fourier high-pass filter on the ASU/DM spot images taken with the ND filter (left) and DM/satellite spot coronagraphic images (right) for different filter sizes; the filtering was skipped for filter size of zero. Vertical profiles of the brighter (black, dashed) and fainter (red, solid) sources in both sets of images, scaled to the peak flux of the brighter source (in thousands of counts). The change in PSF morphology due to the filtering is independent of brightness.

Unlike the previous analysis where the two ratios were computed by fitting a two-dimensional Gaussian, we instead opted to use PSF fitting. This was motivated by the non-Gaussian nature of

GPI's PSF, and the fact that the ND images and coronagraphic images have different PSFs (as the latter is apodized), which may cause biases in the two-dimensional Gaussian fit that may be different for the apodized and non-apodized PSF. The ratio between the central ASU PSF and the average of the four DM spots was calculated within each wavelength slice of each ND image, and similarly for the average of the four DM spots and four satellite spots (or four second-order satellite spots) in each wavelength slice of each coronagraphic image. The objective function minimized using a Nelder-Mead downhill simplex algorithm was:

$$f(a,b) = \sum_{r_i < c} [10^a X_i - (Y_i - b)]^2$$

where X is the brighter source (the ASU in the ND images or the average of the four DM spots in the coronagraphic images), Y is the fainter source, a is a scaling factor (logarithmic to enforce positive values), and b is a DC offset term. The summation is computed over all pixels i, where the radius r_i is less than the fitting radius c. This process was repeated for a number of different fitting radii (0.8-3 λ/D), high-pass filter sizes (including no high pass filter, see Table 3), with and without a DC offset term for the fainter source, and with and without a mask on the central pixel to account for potential non-linearity and saturation. For most of the data taken in 2017, the phase of the sine wave on the DM was modulated to account for non-common path aberrations causing speckles to interfere with the faint DM spots (see Section 7). Images from the four phase angles were averaged together before performing the PSF fitting.

Table 3 : Fourier high-pass filter (HPF) sizes used for each bandpass. Column headings denote the HPF radii in λ/D units, where λ is the central wavelength of the bandpass. The table entries are the corresponding radii in Fourier space; in the image plane the size in pixels is $281/n$. For comparison, the rightmost column lists the standard GPIES campaign data processing HPF parameters for each bandpass.

	No HPF	**11.3 λ/D**	**9.1 λ/D**	**7.5 λ/D**	**6.5 λ/D**	**5.7 λ/D**	**†**
Y	0	12.6	15.7	18.9	22.0	25.2	10.0 (14.3 λ/D)
J	0	10.7	13.3	16.0	18.7	21.4	10.0 (12.1 λ/D)
H	0	8.0	10.0†	12.0	14.0	16.0	10.0 (9.1 λ/D)
K1	0	6.5	8.1	9.7	11.3	12.9	10.0 (7.3 λ/D)
K2	0	5.9	7.3	8.8	10.3	11.7	10.0 (6.7 λ/D)

†Nominal value used to process campaign observations

Examples of the PSF fitting process are shown for a single wavelength slice for an ND image in Figure 5, and a coronagraphic image in Figure 6. The satellite spot ratio for each wavelength slice was computed by performing this PSF fitting analysis on a temporally-averaged data cube, while the uncertainties were estimated by taking the standard deviation of the ratios calculated from the individual images, normalized by the square root of the number of images. As the pupil plane grid width is achromatic the final satellite spot ratio can be calculated by simply taking the average of the ratios computed in each wavelength slice.

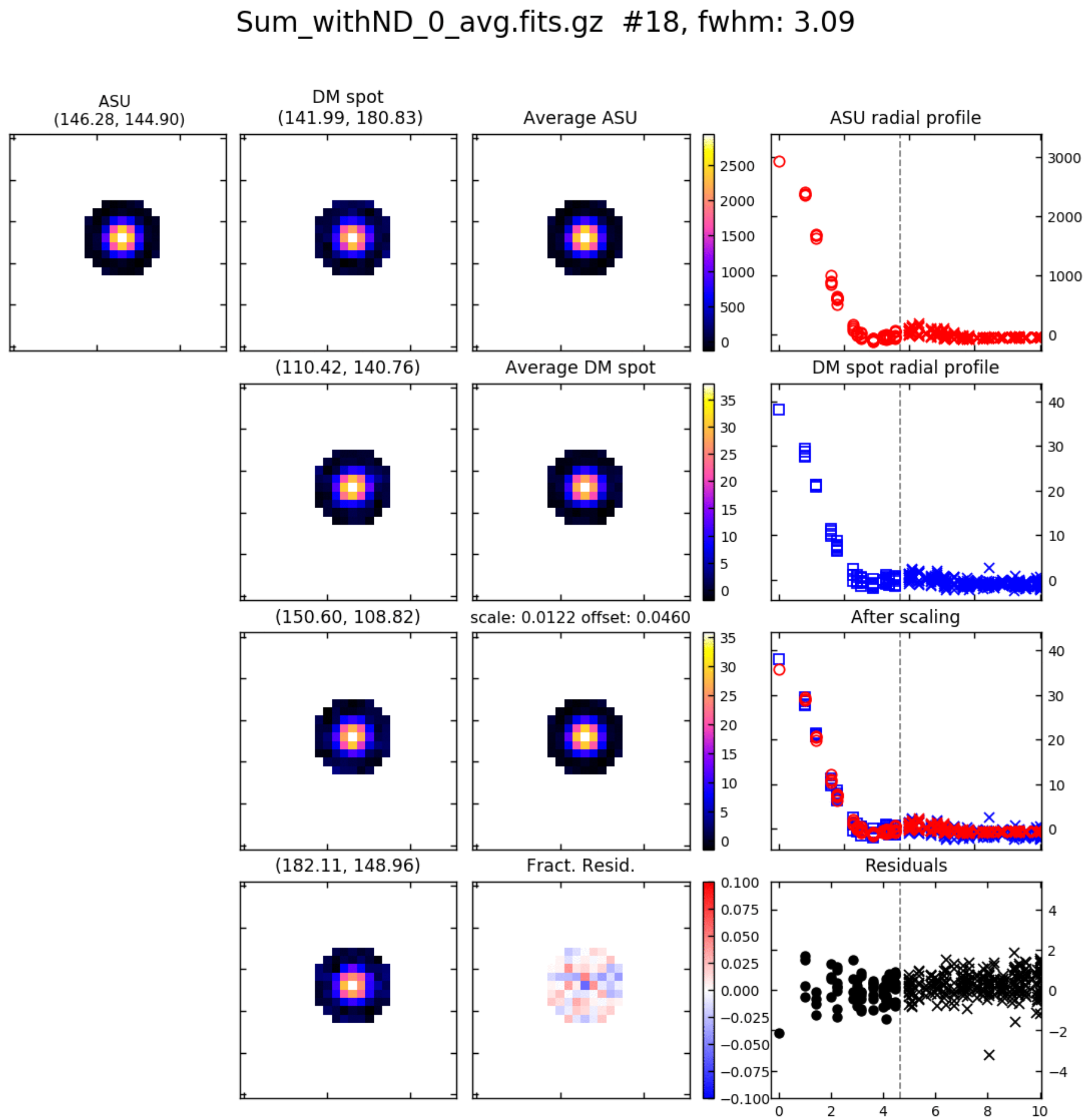

Figure 5: PSF fitting procedure for one wavelength slice of one cube taken with the ND filter from a 2017 H/Hapod dataset (mode 13, 17°, averaged phase). The left column shows the ASU PSF core (in the center of the image), the next column shows the four DM spots generated by the sine wave. The ASU PSF is again shown in the top row of the third column, followed by the average of the four DM spots, the scaled version of the ASU PSF, and the fractional residual after the two are subtracted (scaled to between -10 and +10%). Pixels beyond the fitting radius were set to NaN. The right column shows the radial profiles of the ASU PSF, average DM spot, both after the scale factor and DC offset are applied, and the corresponding residuals in data numbers. Data points included within the minimization are shown as open circles and squares, those beyond the fitting radius (grey dashed line) are plotted as crosses.

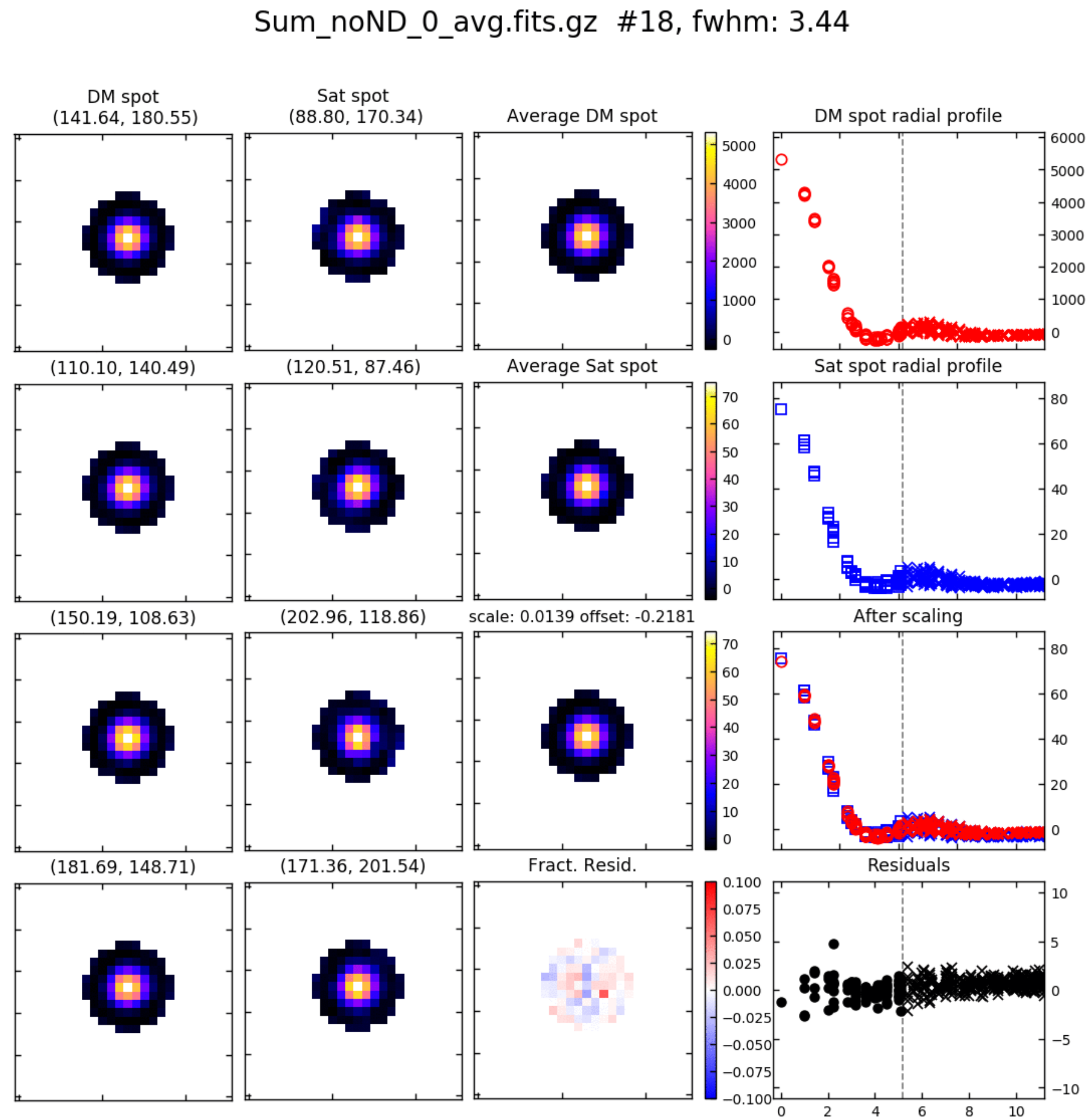

Figure 6: As Figure 4 but for the coronagraphic images. Rather than comparing the central ASU PSF to the average of four DM spots, the average of the four (significantly brighter) DM spots is compared to the average of the four satellite spots. The significantly larger FWHM at the same wavelength is due to the effects of the pupil apodization on the PSF.

5. Fitting Validation

We validated the PSF fitting algorithm using simulated GPI data generated with *poppy*. An ND image was simulated by replicating the central PSF, multiplying by a known scale factor (0.014), and injecting these scaled copies at similar radial and azimuthal positions as in the lab data. Noise was simulated using a Gaussian distribution (Figure 7, top row), as well as three different dark frames added to simulate variations in the noise over the image (one of which is shown in Figure 7, bottom row). This extra noise was injected to at different amplitudes to validate the fitting procedure over a range of signal to noise ratios.

The PSF fitting algorithm was applied to these simulated datasets, generated with a range of S/N values (5 to 1,000). For S/N > 10, the fractional error between the recovered flux ratio and the known scale factor (0.014) was < 2.5%. See Figure 8.

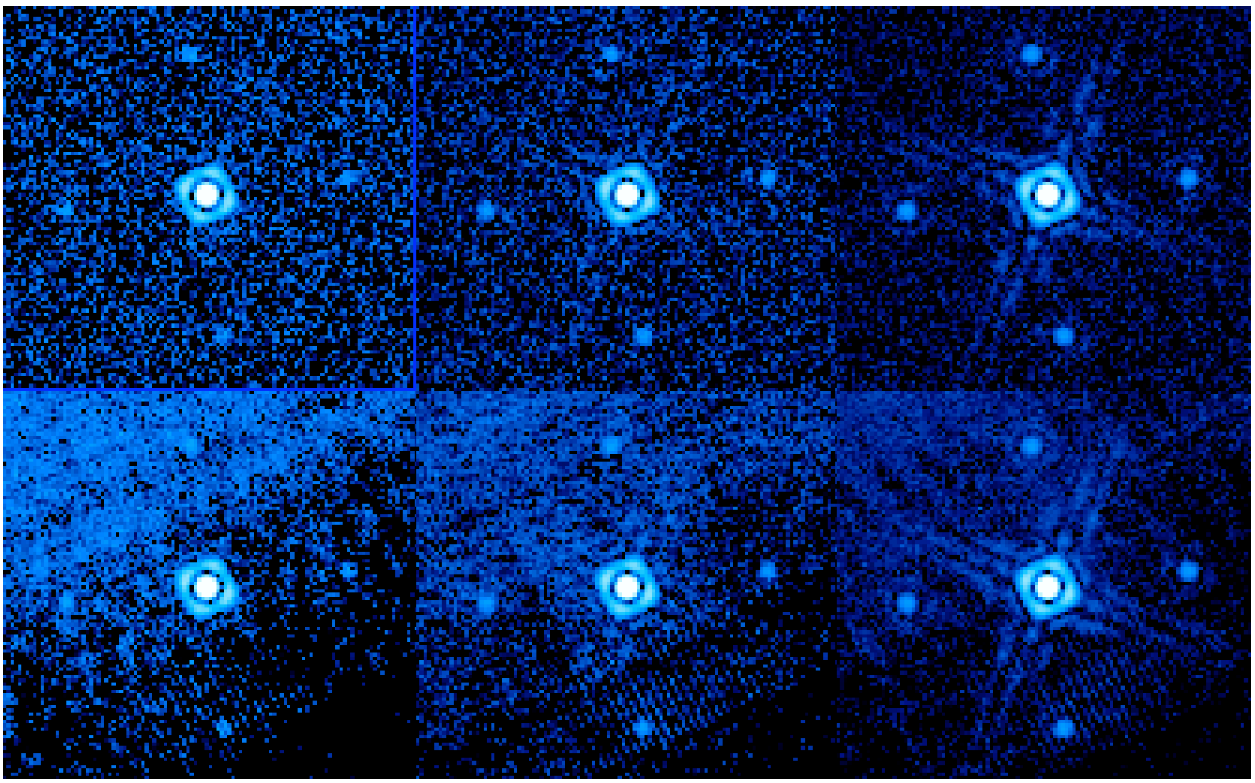

Figure 7: poppy simulations of the images taken with the ND filter showing the ASU in the center, and the four DM spots for two different noise realizations (Gaussian in the top row, using a dark frame in the bottom row). The noise was injected at different amplitudes; S/N of 5 (left), 10 (middle), and 25 (right) relative to the peak amplitude of the DM spots.

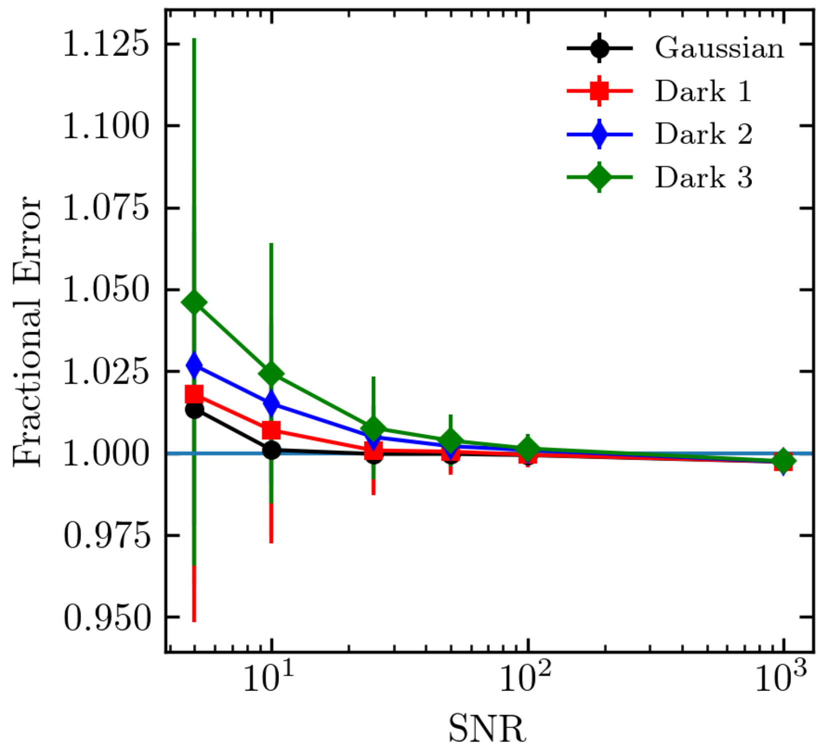

Figure 8: Fractional error in the recovered ASU to average DM spot ratio as a function of signal-to-noise ratio for simulated datasets with four different noise realizations. At SNR>10, the fractional error is < 2.5%.

6. Discrepancy Between Original Calibration and Repeat Measurement

The initial goal was to confirm that we could reproduce the nominal satellite spot flux ratio by applying the PSF fitting procedure described previously to the existing 2013 dataset, and that this result could be repeated with a new set of experimental data obtained. The satellite spot ratio measured from a re-analysis of the 2013 dataset was consistent with the nominal value ($\sim 2 \times 10^{-4}$), but the repeat of the experiment yielded a significantly lower value of 1.6×10^{-4} (Figure 9). While a significant change in the satellite spot ratio could have occurred due deterioration of the physical structure of the apodizer, this was considered unlikely. Repeat measurements in early-2017 were taken in which the spatial frequency and rotation of the sine wave applied on the DM to generate the bright DM spots was varied. The results of the analysis of these data showed a significant change in the satellite spot ratio as a function of the sine wave parameters (Figure 9), a range far larger than the stated uncertainties on the nominal ratio. The impact of varying the fitting radius and high-pass filter size is demonstrated in Figure 10, showing that significant changes in these parameters only leads to a relatively small change in the measured satellite spot ratio (<10%), and cannot explain the observed discrepancy.

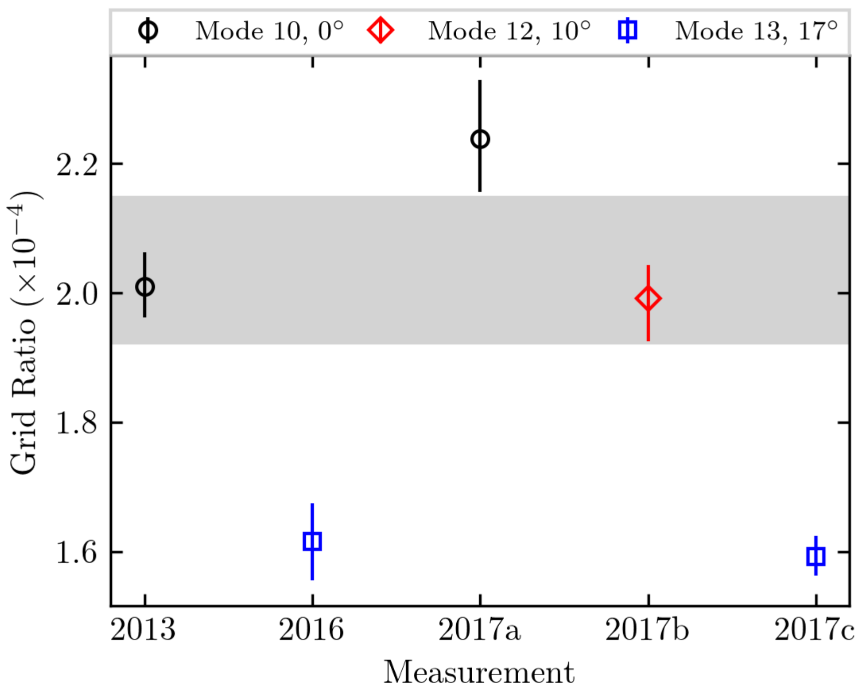

Figure 9: H-band satellite spot ratio for the five datasets taken with different DM sine wave configurations with no phase modulation (see §7). The nominal ratio used to-date is denoted by the grey shaded region. The discrepancy between the 2013 and 2016 datasets was originally thought to be due to the different position of the spots in the IFS image, and repeat measurements in 2017 at three different positions seemed to confirm this.

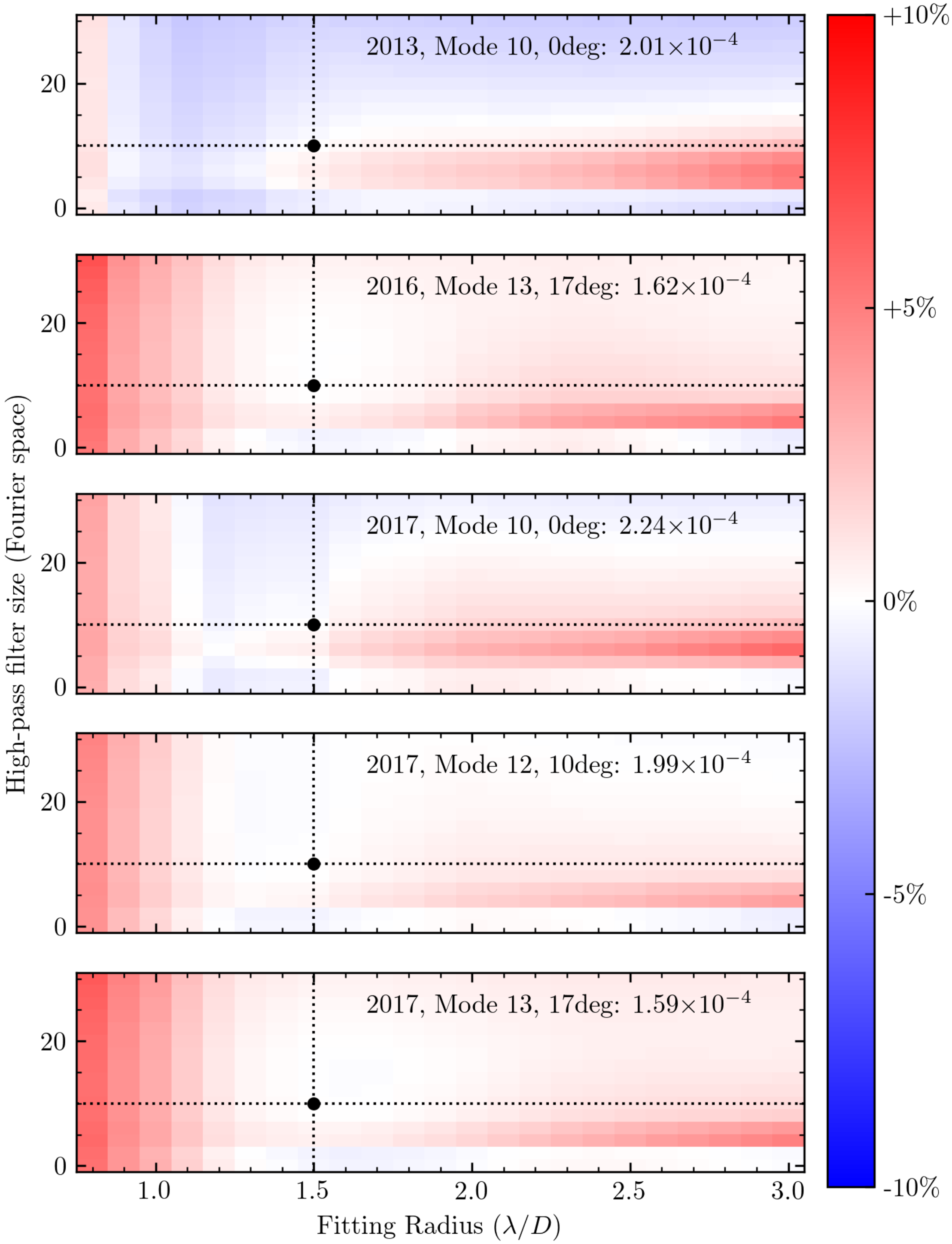

Figure 10: Effect of varying fitting radius and the size of the high-pass filter on the final satellite spot ratio. Fitting radii are in units of λ/D, and the size of the high-pass filter is in the Fourier domain; in the image plane the size in pixels is 281/n. The color scale shows the percent deviation from the ratio computed at the nominal fitting radius (1.5 λ/D) and filter size (10, or 28.1px), both of which are marked by the dotted lines. Each panel shows the analysis for the datasets taken in 2013, 2016, and early-2017. The frequency of the sine wave on the DM, its rotation, and the mean satellite spot ratio are given. Note the significant differences in the satellite spot ratio as a function of the configuration of the DM sine wave.

7. Non-common Path Aberrations

A significant difference between the 2013 and original 2016 datasets that was initially overlooked was the difference in morphology of the DM spots as a function of the spatial frequency and rotation of the sine wave on the tweeter (Figure 11). At the lowest spatial frequency tested (mode 10), the first and second (counting counter-clockwise from the top) DM spots appeared significantly distorted relative to the central ASU and the other two DM spots. This effect was not as prominent in the 2013 data, which was taken with similar instrument and sine wave configurations, with the DM spots appearing relatively symmetric. The PSF distortions were still present at higher spatial frequencies in the 2017 datasets (modes 12 and 13), although less pronounced.

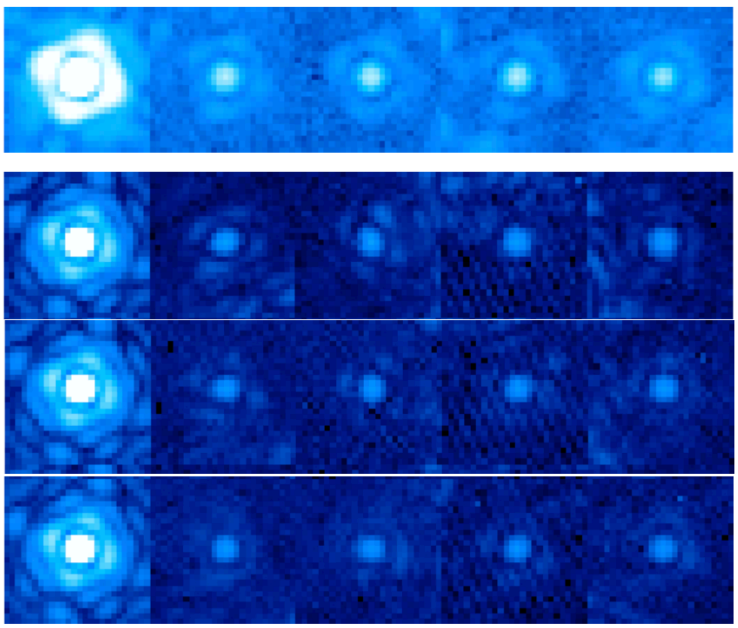

Figure 11**:** Morphology of the ASU (left column) and DM spots (right columns) for the 2013 dataset (top row) and the datasets taken in 2017 with different sine wave configurations (bottom rows). The DM spots are clearly deformed relative to circular, possibly due to interference with the bright speckle field from the ASU in these non-coronagraphic images.

It was hypothesized that the DM spots may be interfering with residual speckles from the bright central ASU (~10^{-2} flux ratio), leading to a significant change in their morphology. This was confirmed in an experiment where we varied the phase of the sine wave applied to the DM from 0°-360° (e.g., a hypothetical actuator at +1μm at 0° phase would be at -1μm at 180° phase). This experiment demonstrated that the brightness and morphology of the DM spots changed significantly with the phase of the sine wave (Figure 12), with peak-to-trough amplitude variations of ~40% (Figure 13). The true flux ratio between the ASU and the average DM spot was calculated by applying the PSF fitting procedure described previously to the average of all 24 data cubes, cancelling out the changes in the morphology induced by constructive and destructive interference (Figure 13). The same ratio was recovered by averaging the four images with a phase of $\phi = 0$, 90, 180, and 270°, a significant reduction in the number of images required per experiment. For all subsequent experiments data were taken at these four phase angles to average out this interference.

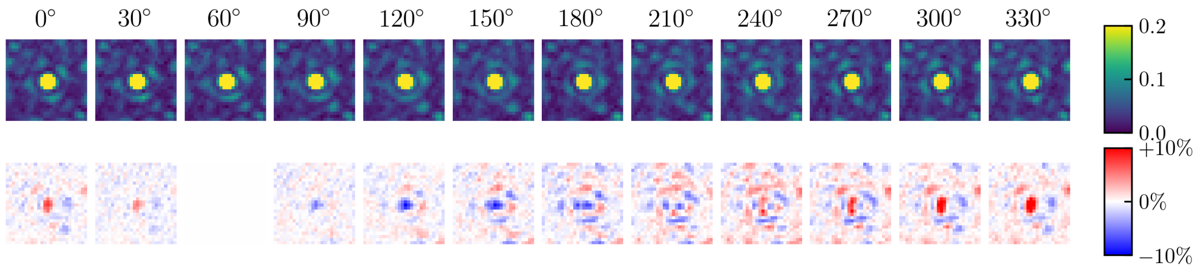

Figure 12: Effect of adjusting the phase (ϕ) of the sine wave on the PSF of the DM spot for 12 different phase angles (top row). The difference ϕ_i-ϕ_{60} (bottom row) demonstrates the significant change in the brightness of the DM spots as a function of the phase of the applied sine wave.

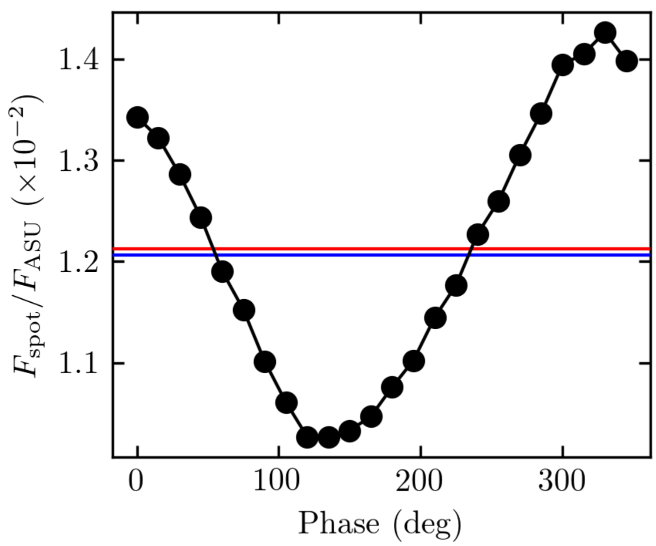

Figure 13: Flux ratio between the ASU and the DM spots as a function of sine wave phase (black points). The ratio calculated from an analysis performed on the average of the 24 data cubes is denoted by the red horizontal line, whilst that performed on the average of the ϕ=0, 90, 180, and 270° data cubes is shown in blue, demonstrating that measurements at four phases is sufficient to recover the true flux ratio.

8. Lab Results

The modified experimental design was used to obtain satellite spot ratio measurements in the following instrument configurations:

Y filter/Y apodizer, Y filter/H apodizer	(2017 August, September)
J filter/J apodizer, J filter/H apodizer	(2017 June)
H filter/H apodizer	(2017 April, June, August)
K1 filter/K1 apodizer, K1 filter/H apodizer	(2017 June)

The PSF fit was only performed in wavelength channels with a high (≳10) SNR detection of the DM spots in the ND image, and the satellite spots in the coronagraphic images. Analysis of the Y-band data was therefore restricted to channels 6-27, J-band to channels 2-34, H-band to channels 18-34, and K1 to channels 6-12. Measurements of the K2 satellite spot ratio are not possible with the ASU due to the low throughput of the fiber beyond ~2μm.

8.1. Y band (w/ Y apodizer)

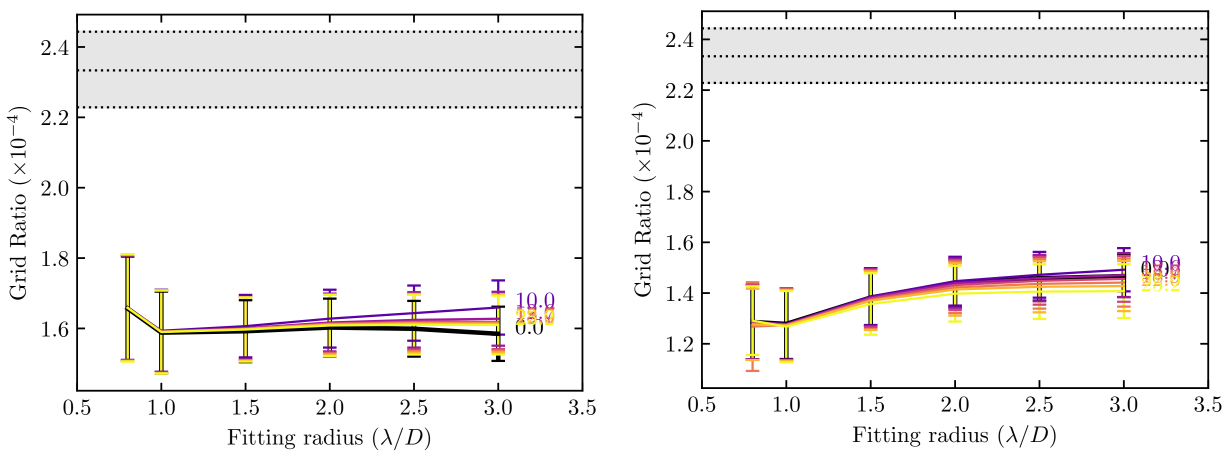

Figure 14: Y-band ratio as a function of fitting radius for fits without high-pass filtering (black) and with varying high-pass filter sizes (colored lines) for the first order (left) and second order (right) satellite spots. The nominal first-order satellite spot ratio is shaded in grey. These fits included a DC offset term, but did not mask the central pixel. The ratio is insensitive to the high-pass filter size, but there is a slight but not significant dependence on the fitting radius for the second-order spots. Data from September 2017.

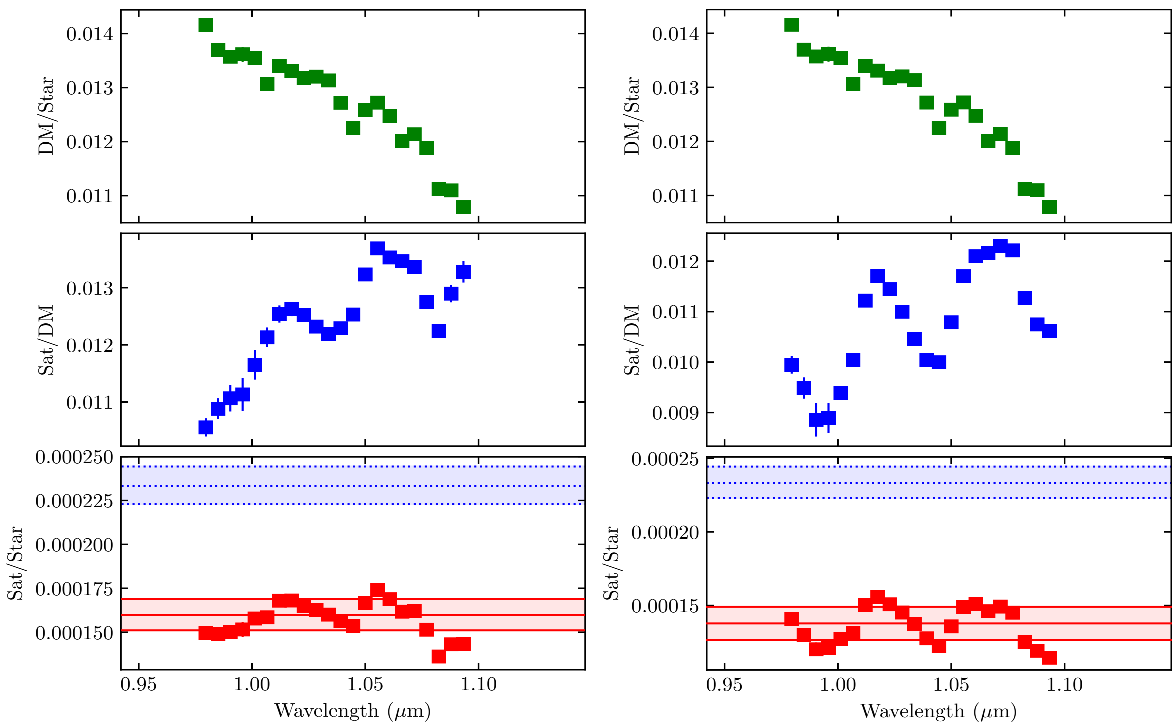

Figure 15: ASU to average DM spot ratio (top), average DM spot to average satellite spot ratio (middle) and final satellite spot ratio (bottom row) as a function of wavelength for the first-order (left) and second order (right) Y-band satellite spots. This fit used a high pass filter size of 15.7 (9.1 λ/D) and a fitting radius of 1.5 λ/D. The nominal first-order ratio shaded in blue. The variation seen in the middle row may be due to the under-sampling of the PSF at Y band.

8.2. Y band (w/ H apodizer)

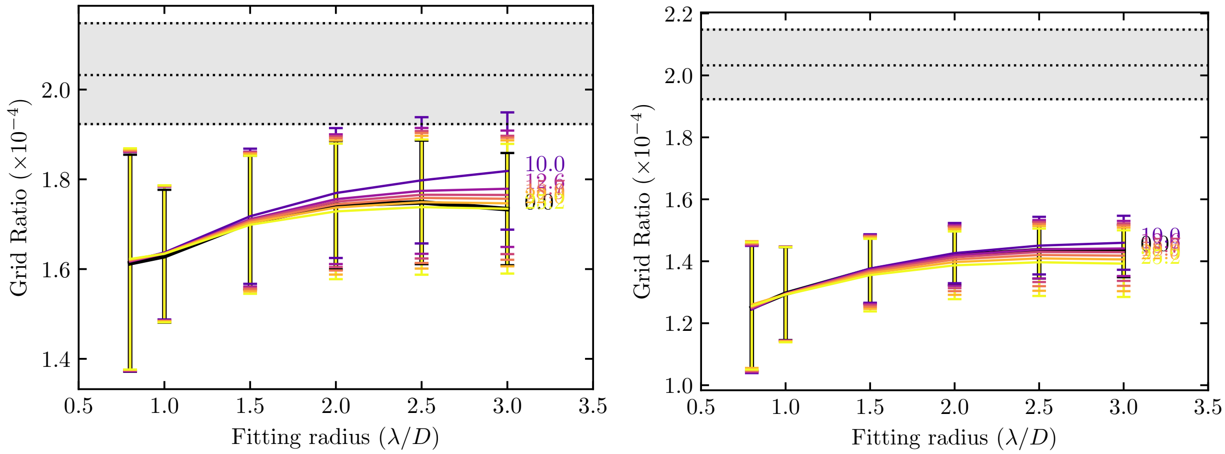

Figure 16: As Figure 14, but for the non-standard Y filter/H apodizer instrument configuration. The nominal ratio shown here is for the H-band apodizer.

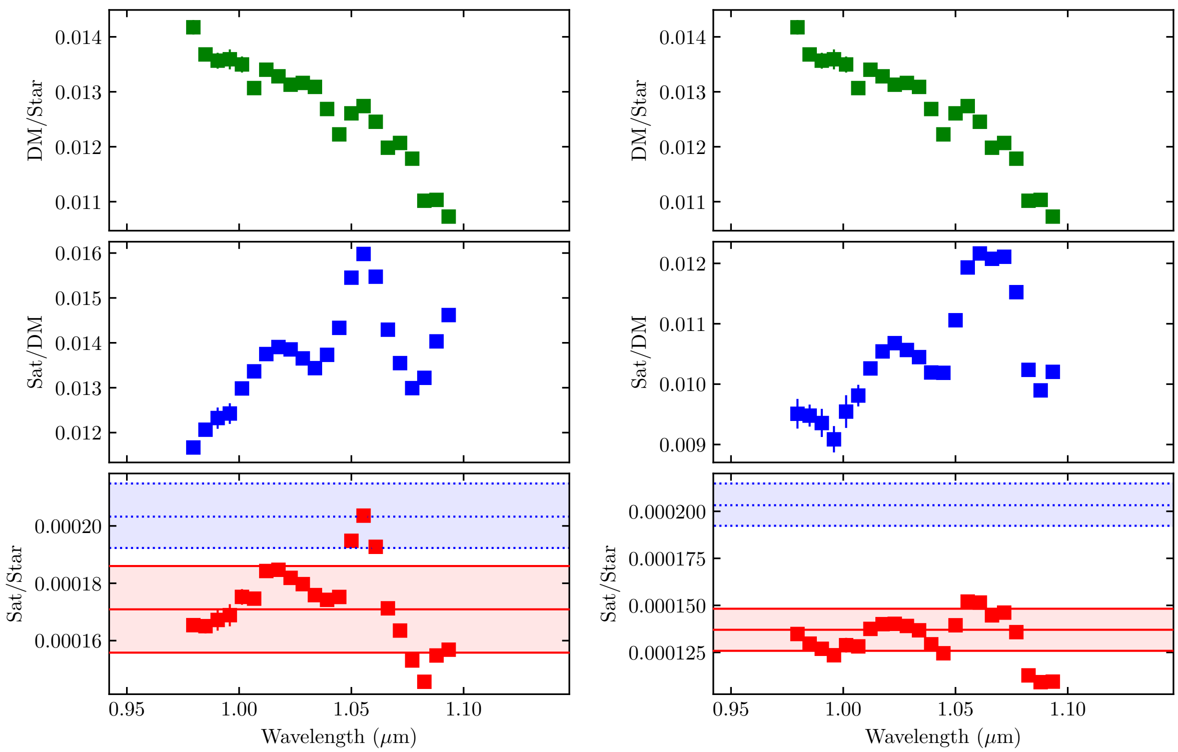

Figure 17: As Figure 15.

8.3. J band (w/ J apodizer)

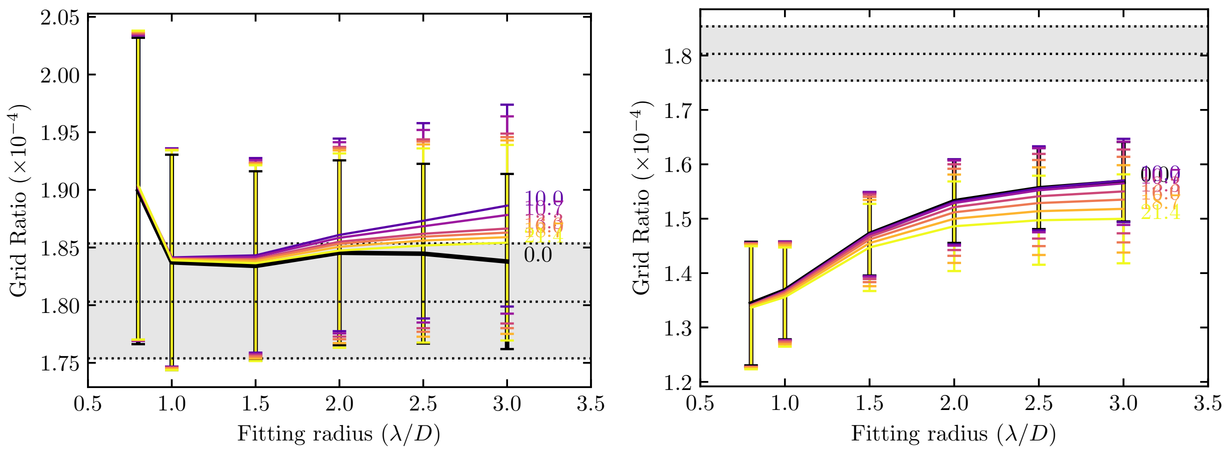

Figure 18: As Figure 14, but for the *J* filter/*J* apodizer instrument configuration.

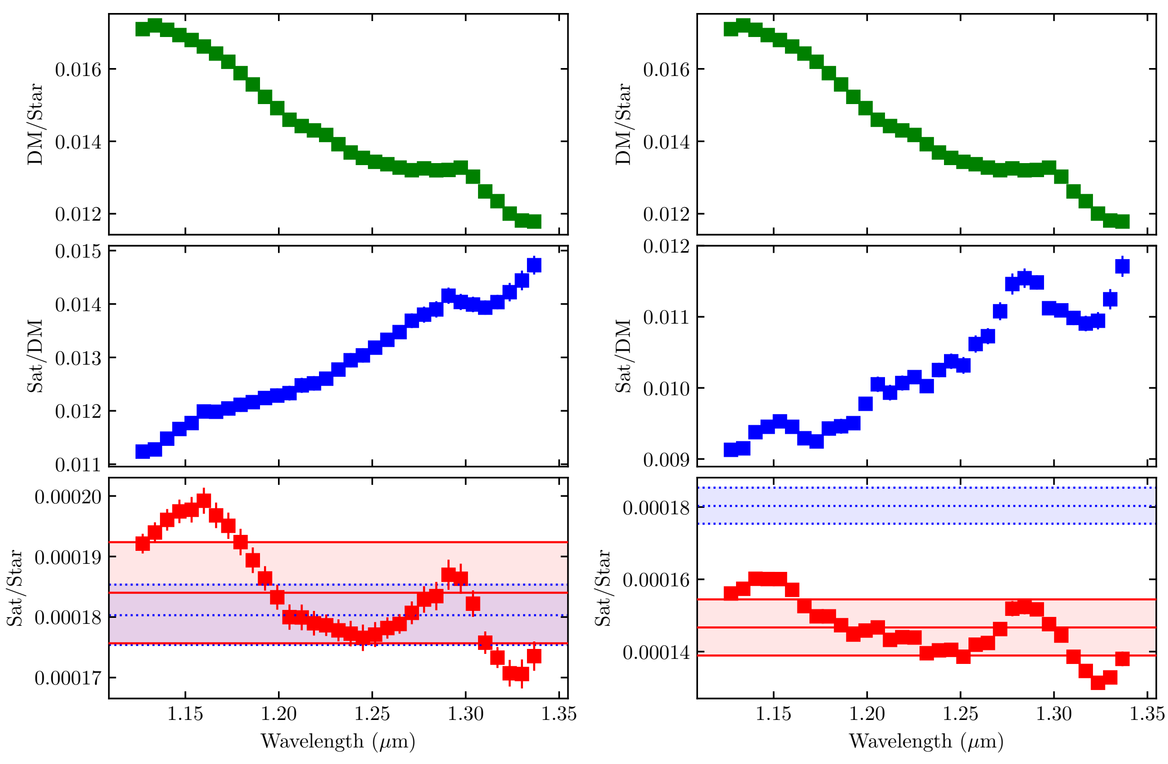

Figure 19: As Figure 15, but with a filter size of 13.3 (again corresponding to 9.1 λ/D).

8.4. J band (w/ H apodizer)

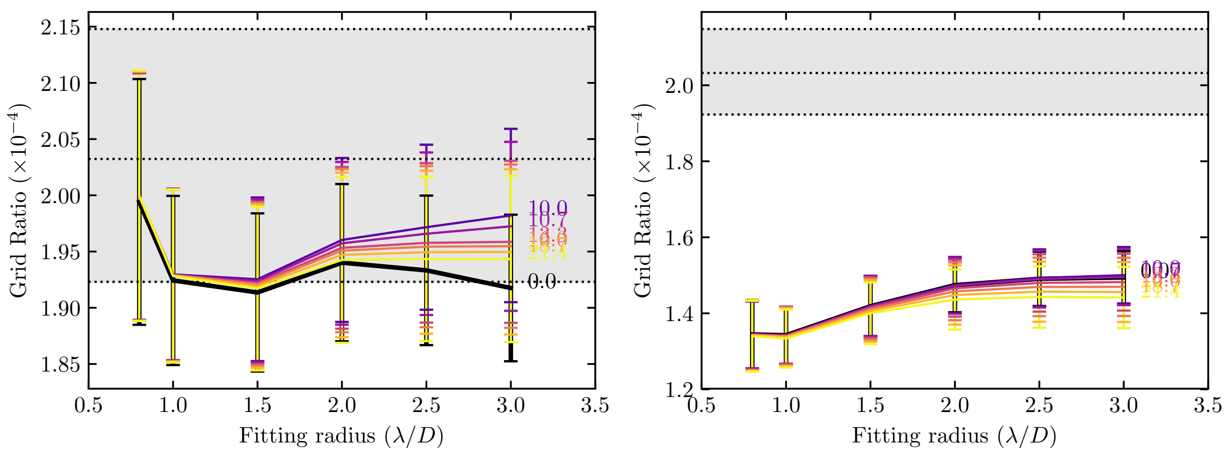

Figure 20: As Figure 14, but for the non-standard J filter/H apodizer instrument configuration.

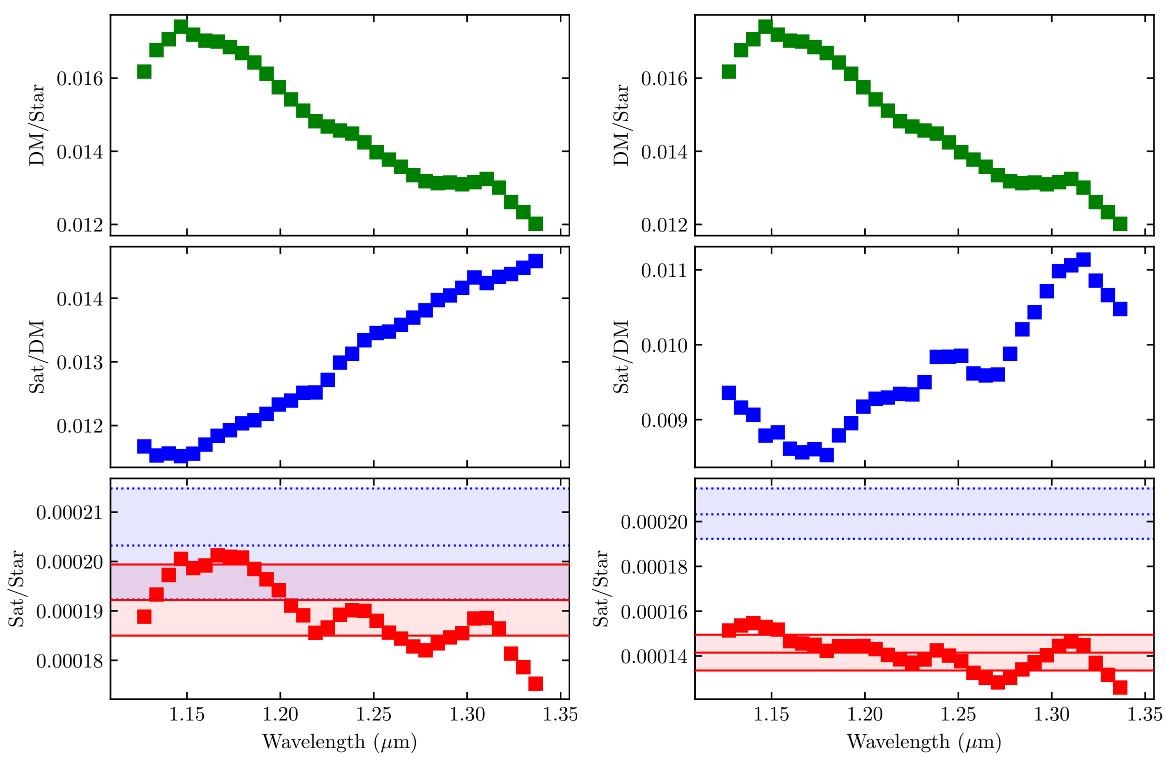

Figure 21: As Figure 15, but with a filter size of 13.3 (again corresponding to 9.1 λ/D).

8.5. H band

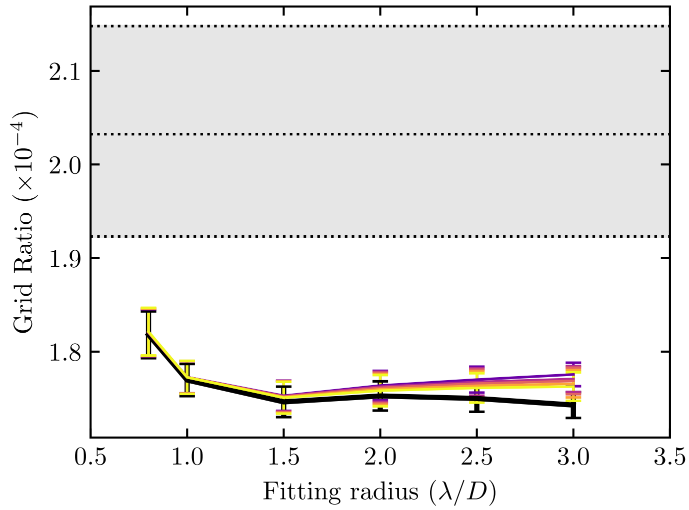

Figure 22: As Figure 14, but for the standard H filter/H apodizer instrument configuration. Second-order spots are not fitted as they fall outside GPI's field of view beyond ~1.5 μm.

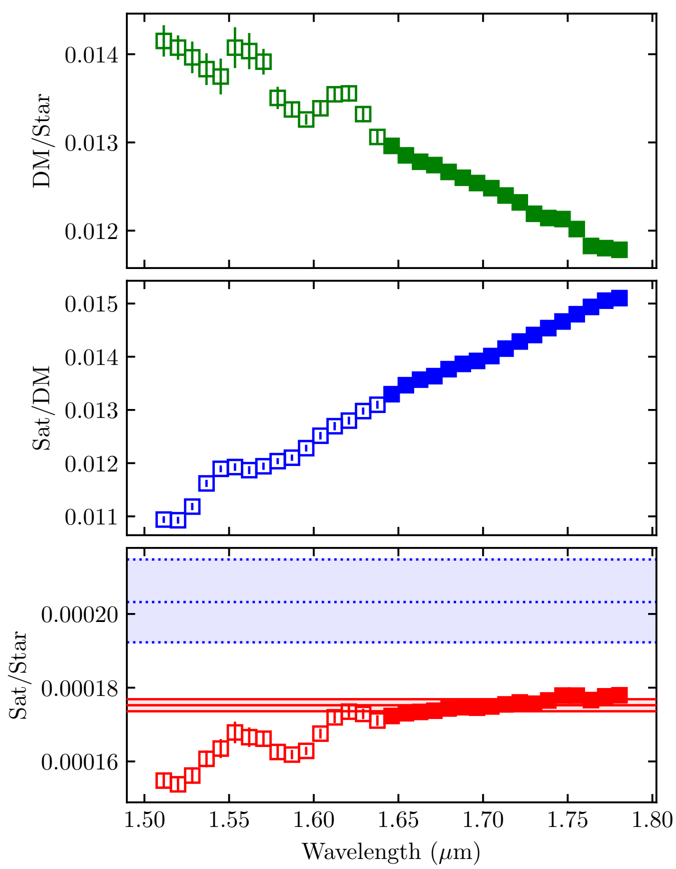

Figure 23: As Figure 15, but with a filter size of 10 (corresponding to 9.1 λ/D). Data points not included in the calculation of the final satellite spot ratio are shown as open symbols. The low S/N of the DM spots in the ND image was causing an overestimate in their flux (as seen in the simulations in Figure 8).

8.6. K1 band (w/ K1 apodizer)

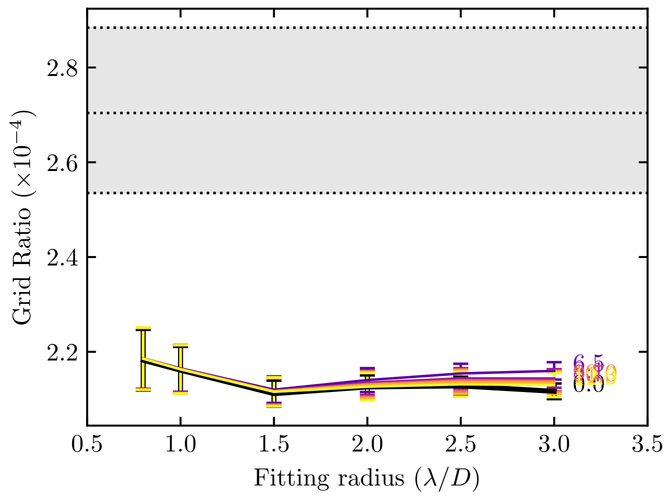

Figure 24: As Figure 14, but for the K1 filter/K1 apodizer instrument configuration. Second-order spots are not fitted as they fall outside GPI's field of view beyond ~1.5 µm.

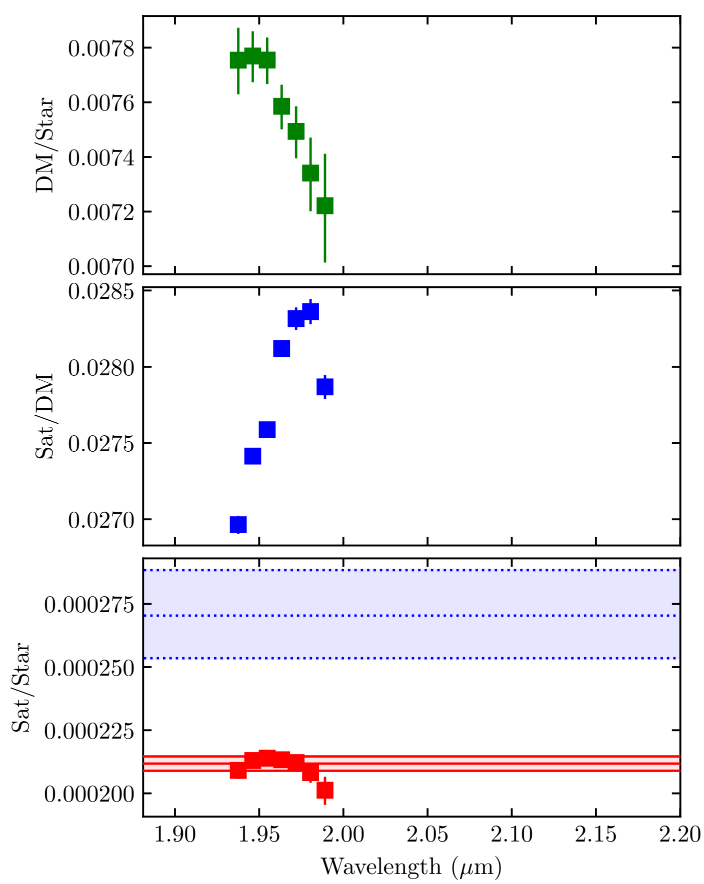

Figure 25: As Figure 15, but with a filter size of 8.1 (again corresponding to 9.1 λ/D). Low throughput of the ASU fiber precluded a measurement of the satellite spot ratio beyond 2.0 µm.

8.7. K1 band (w/ H apodizer)

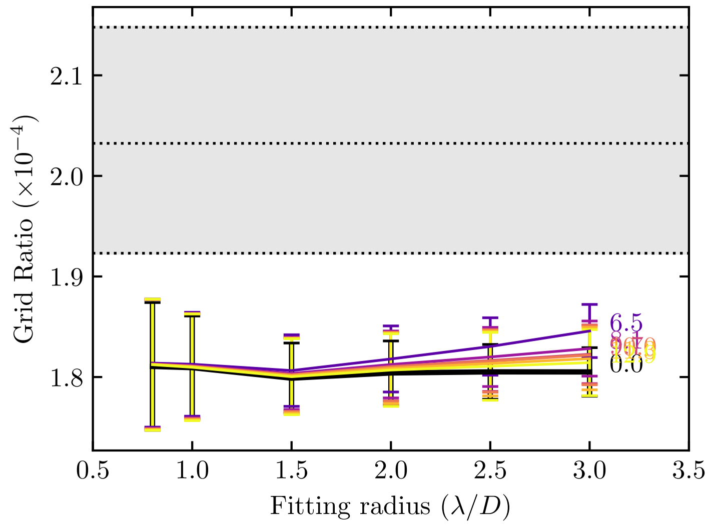

Figure 26: As Figure 14, but for the non-standard K1 filter/H apodizer instrument configuration.

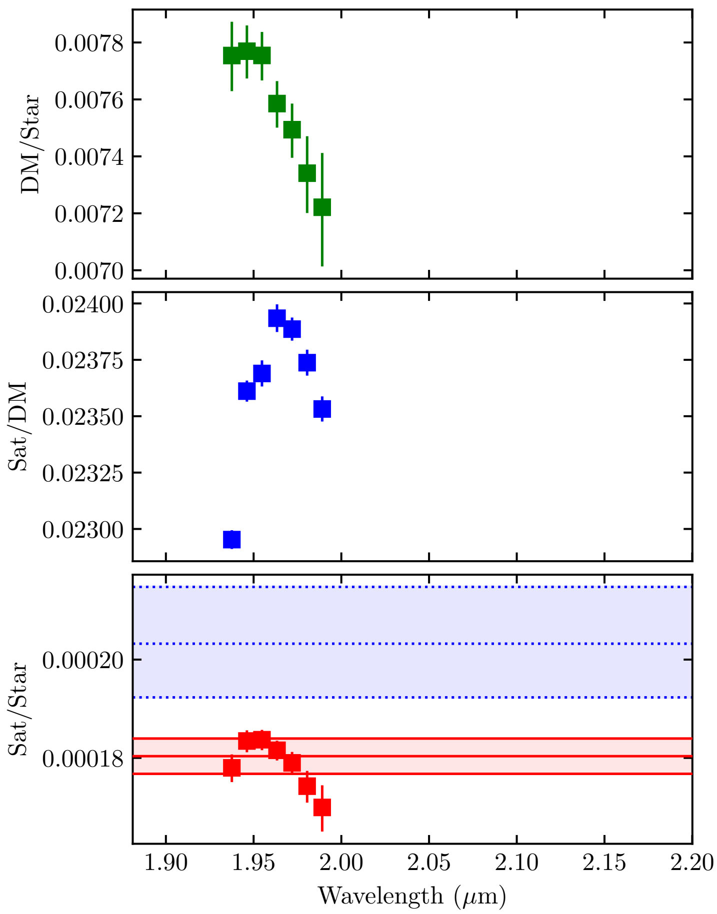

Figure 27: As Figure 15, but with a filter size of 8.1 (again corresponding to 9.1 λ/D).

9. New Satellite Spot Ratios

Table 4: Adopted satellite spot ratios

Filter	Apodizer	Order	Ratio (x10^{-4})	Δm	Change
Y	Y	1	1.60 ± 0.09	9.49 ± 0.06	-31%
Y	Y	2	1.42 ± 0.12	9.62 ± 0.10	n/a
Y	H	1	1.71 ± 0.15	9.42 ± 0.10	n/a
Y	H	2	1.37 ± 0.11	9.66 ± 0.09	n/a
J	J	1	1.84 ± 0.08	9.34 ± 0.05	+2%
J	J	2	1.47 ± 0.08	9.66 ± 0.06	n/a
J	H	1	1.92 ± 0.07	9.29 ± 0.04	n/a
J	H	2	1.41 ± 0.08	9.62 ± 0.06	n/a
H	H	1	1.74 ± 0.03	9.40 ± 0.02	-15%
K1	K1	1	2.12 ± 0.03	9.19 ± 0.01	-22%
K1	H	1	1.80 ± 0.04	9.36 ± 0.02	n/a

Table 5: Repeat measurements

Filter	Apodizer	Order	Date	Ratio (x10^{-4})	Δm
Y	Y	1	2017-08-11	1.62 ± 0.07	9.48 ± 0.05
Y	Y	1	2017-09-10	1.60 ± 0.09	9.49 ± 0.06
Y	Y	2	2017-08-11	1.42 ± 0.12	9.62 ± 0.10
Y	Y	2	2017-09-10	1.38 ± 0.11	9.65 ± 0.09
H	H	1	2017-04-17	1.76 ± 0.03	9.39 ± 0.02
H	H	1	2017-06-16	1.75 ± 0.02	9.39 ± 0.01
H	H	1	2017-08-11	1.72 ± 0.01	9.41 ± 0.01

10. On-sky Verification

The revised measurements presented in Table 4 were verified by observing a known binary star with a flux ratio close to 1:100, analogous to the flux ratio of the DM spots in the experiments described previously. Three such binary systems were identified, HD 74341 B, HR 5625, and HD 215768. The primary objective was to verify the H-band ratio, but measurements were also obtained with the K1 filter with both the K1 and H apodizer.

10.1. H-band data

HD 74341 B

Results for the analysis of the HD 74341 B (Figure 28) H-band data from 2018-03-08 are shown in, left column. The derived H-band ratio is consistent with the adopted ratio given in Table 4. A repeat measurement of this system on 2018-03-26 yielded a lower derived satellite spot ratio (Figure 29 and Figure 30, right column), a ~1-σ discrepancy between the two datasets. The residual maps for these datasets suggest that the primary (HD 74341 B) is itself a tight binary (Figure 42), which may be the cause of this discrepancy.

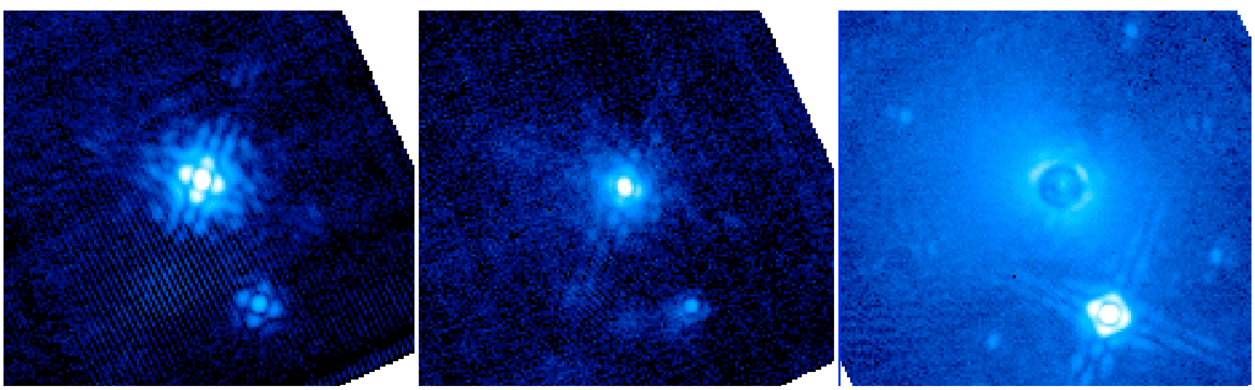

Figure 28: HD 74341 B observed in H-band with three instrumental configurations: (left) with the oversized Lyot mask used to prevent the primary from saturating, the Lyot mask should cause no field-dependent change in throughput, (middle) with the ND filter, and (right) in the full H-band coronagraphic mode.

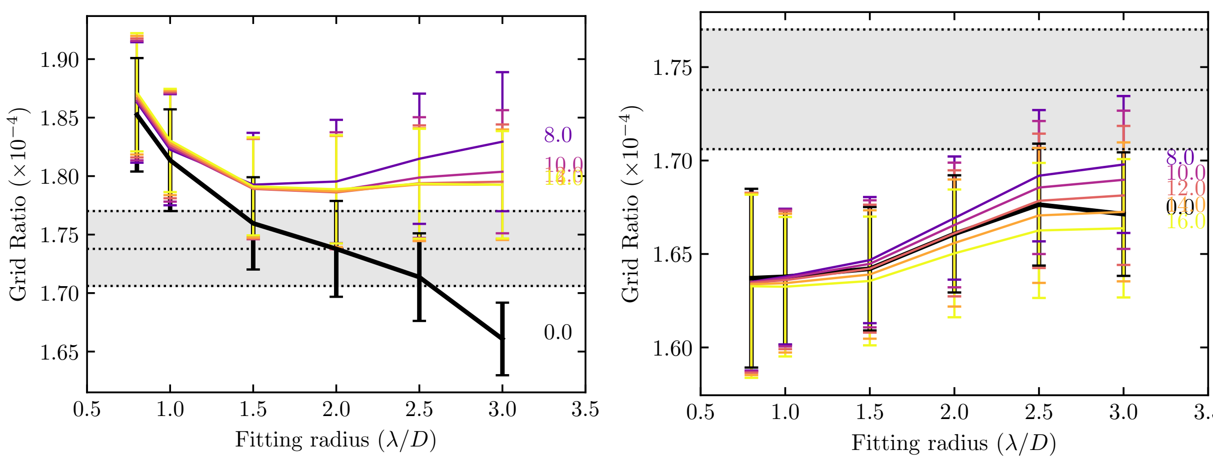

Figure 29: H-band satellite spot ratio derived from observations of HD 73431 B on 2018-03-08 (left) and 2018-03-26 (right) as a function of fitting radius for fits without high-pass filtering (black) and with varying high-pass filter sizes (colored lines). These fits included a DC offset term, but did not mask the central pixel. The new adopted satellite spot ratio in Table 4 is plotted as the grey shaded region. The two measurements are inconsistent at the 2-σ level (note the different y-axis range, and only the 2018-03-08 dataset is consistent with the data obtained with the adopted ratio given in Table 4.

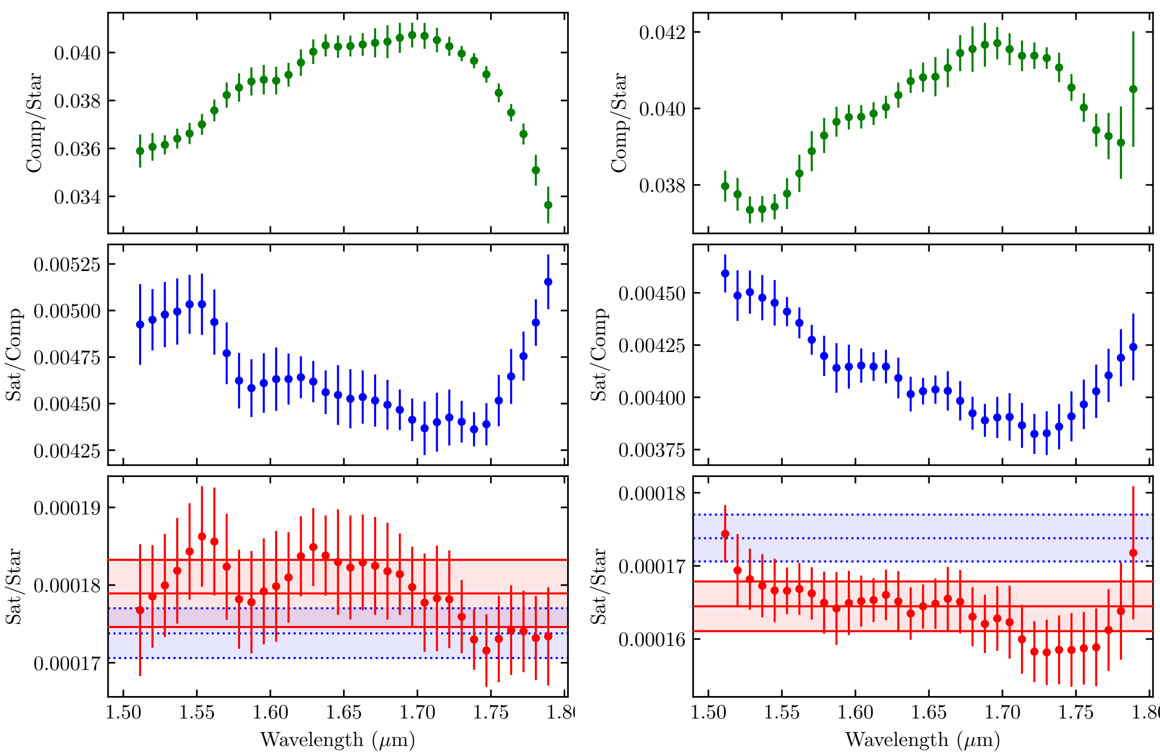

Figure 30: Flux ratio between star and companion (top), flux ratio between companion and average of the four satellite spots (middle) and derived satellite spot ratio (bottom row) as a function of wavelength for the 2018-03-08 (left) and 2018-03-26 (right) datasets. These fits used a high pass filter size of 10.0 (9.1 λ/D) and a fitting radius of 1.5 λ/D. The adopted satellite spot ratio in Table 4 is plotted as the blue shaded region, consistent with the first epoch, but discrepant with the second.

HR 5625

The results for the H-band data of HR 5625 obtained on 2018-03-09 (Figure 31 and Figure 32) are shown in Figure 33 and Figure 34. This dataset suffered from an effect seen during low-wind conditions where a strong diffraction spike interferes with the upper-left and lower-right satellite spots (Figure 32). To mitigate this effect, the fit was limited to the upper-right and lower-left satellite spots. The unocculted dataset also suffered from non-linearity in the core of the PSF of the primary at shorter wavelengths, so the analysis was further limited to wavelength slices 24 through 35 (> 1.7 μm).

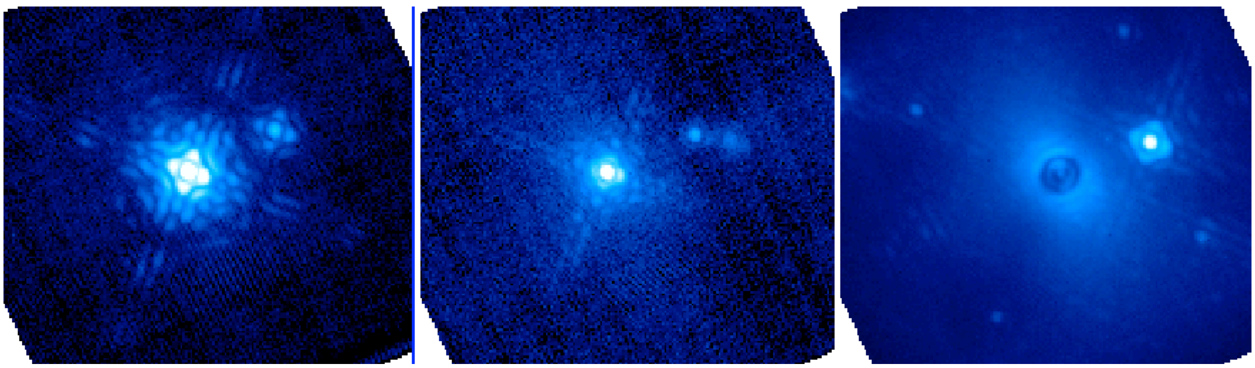

Figure 31: As Figure 28, but for HR 5625.

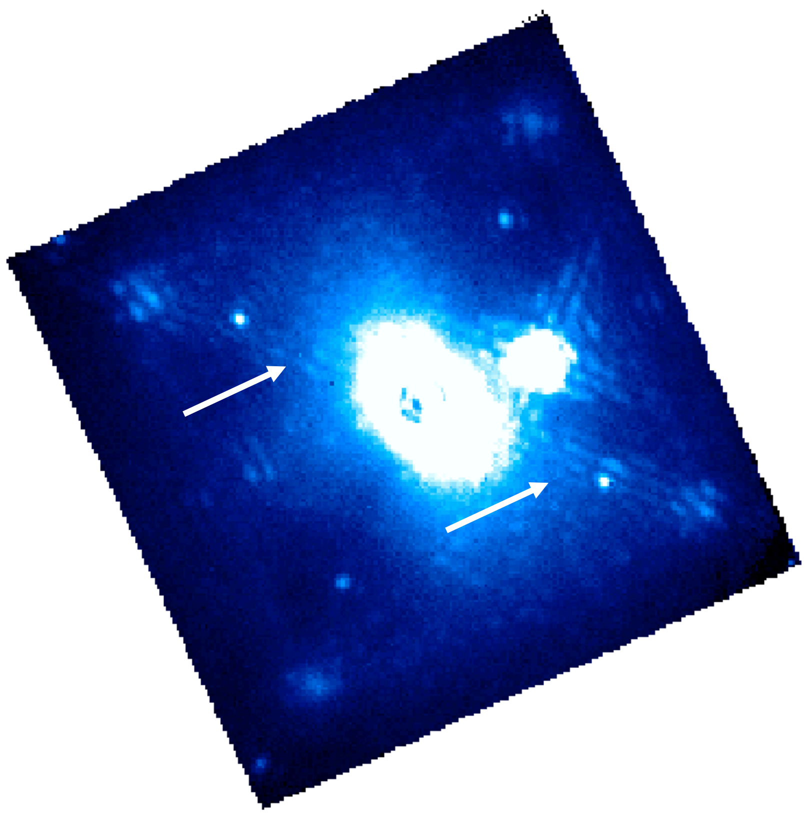

Figure 32: Coronagraphic image of HR 5625 showing interference between the upper left/lower right satellite spots and a diffraction spike (indicated), thought to be GPI's equivalent of the low-wind effect seen in SPHERE observations.

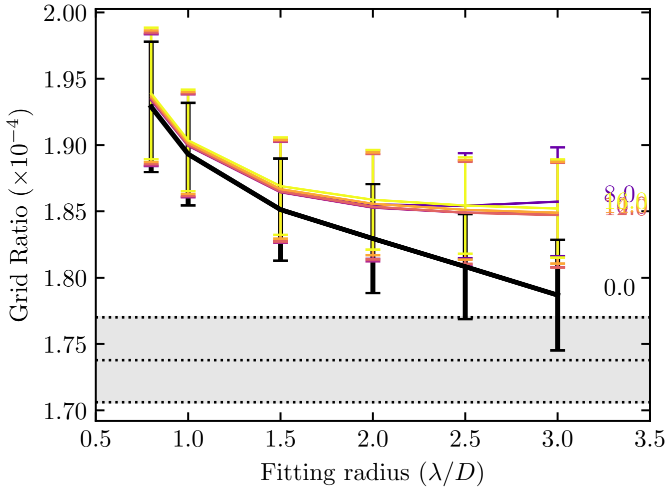

Figure 33: As Figure 29, but for HR 5625 using only the lower-left and upper-right satellite spots and wavelength channels 24 through 35. The adopted ratio from Table 4 is denoted by the shaded grey region.

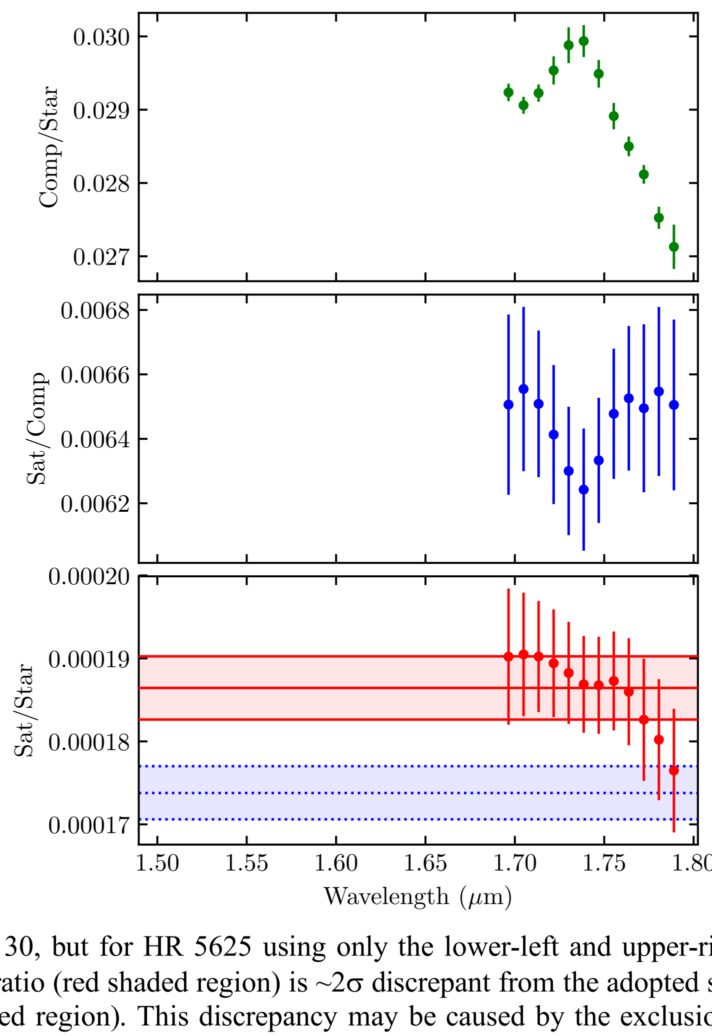

Figure 34: As Figure 30, but for HR 5625 using only the lower-left and upper-right satellite spots. The derived satellite spot ratio (red shaded region) is ~2σ discrepant from the adopted satellite spot ratio given in Table 4 (blue shaded region). This discrepancy may be caused by the exclusion of the upper-left and lower-right satellite spots in the analysis.

HD 215768

HD 215768 was the third calibration binary observed in an attempt to verify the H-band satellite spot ratio. Data were obtained on 2018-07-21 under relatively poor, variable conditions (Figure 35). The results from this dataset are shown in Figure 36 and Figure 37, with the derived satellite spot ratio being consistent with the adopted ratio given in Table 4.

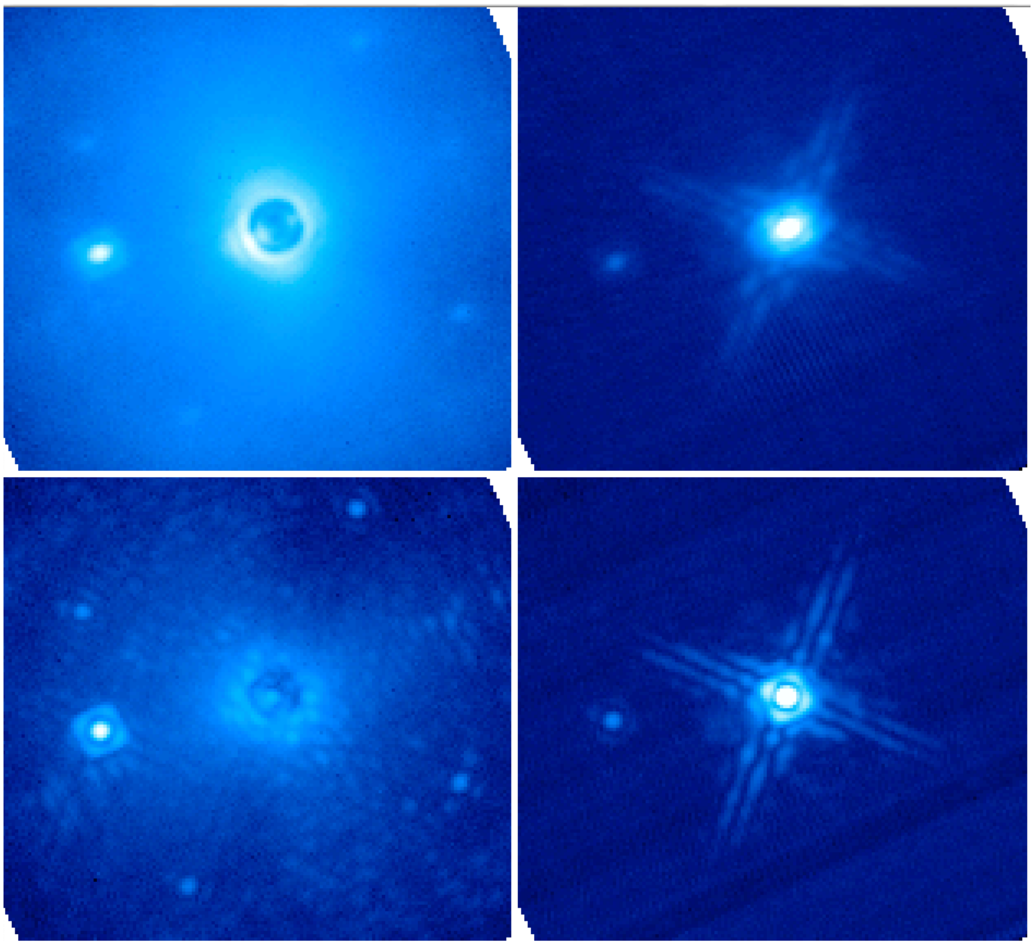

Figure 35: HD 215768 observed in H-band in unblocked mode (left column) and coronagraphic mode (right column) on 2018 July 21 (top row) and 2018 November 21 (bottom row). Observing conditions were significantly better on the second attempt.

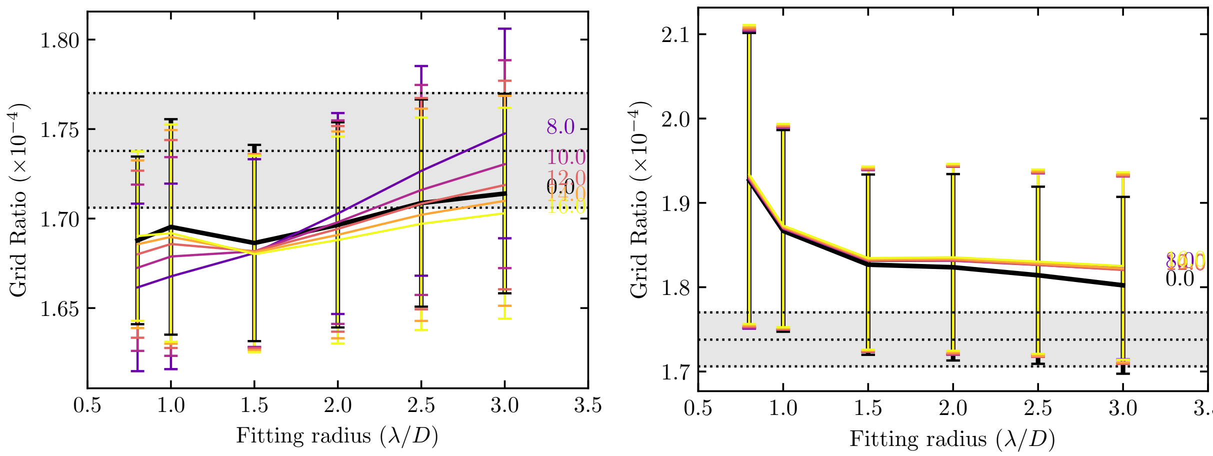

Figure 36: As Figure 29, but for HD 215768 from 2018 July (left) and 2018 November (right). Both measurements are 1σ consistent with the adopted ratio given in Table 4.

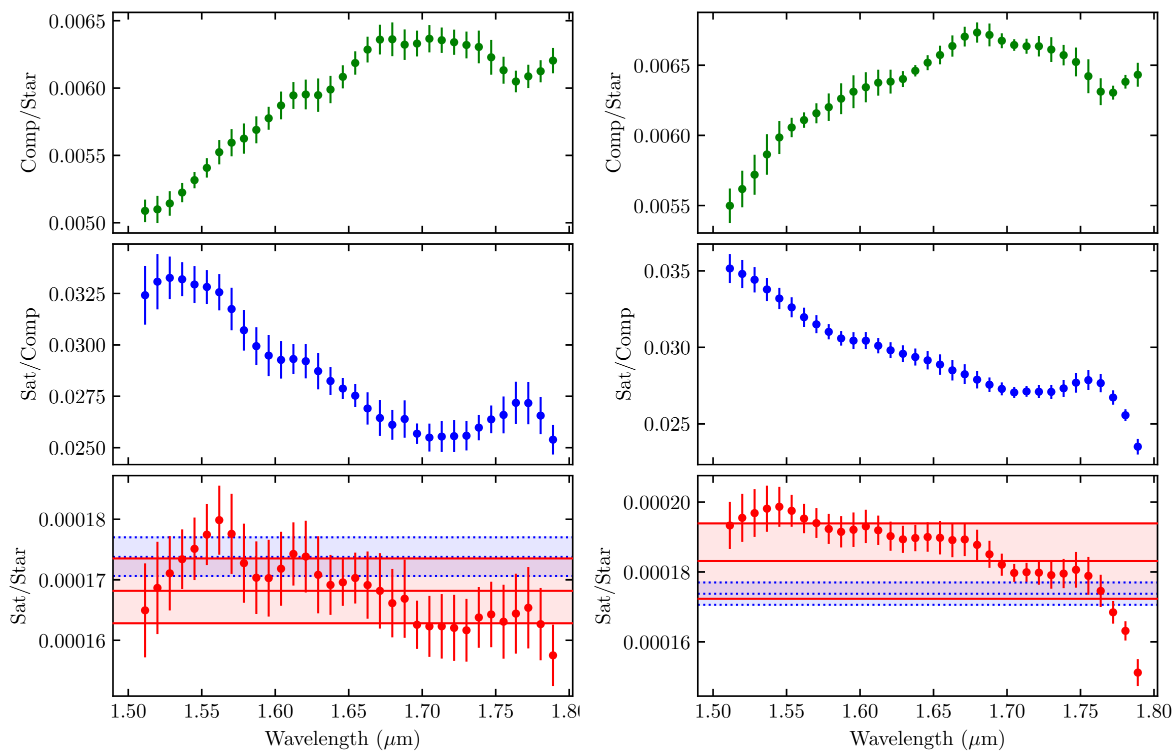

Figure 37: As Figure 30, but for HD 215768 from 2018 July (left) and 2018 November (right). The derived satellite spot ratio (red shaded region) is consistent with the adopted satellite spot ratio given in Table 4.

10.2. K1-band data

HD 74341 B was also observed with the K1 filter on 2018-03-25 with both the H and K1 apodizers (Figure 38). The results of the analysis of these data are shown in Figure 39 and Figure 40. The data obtained with the K1 apodizer are inconsistent with the adopted satellite spot ratio given in Table 4, whereas the H apodizer dataset agrees (albeit with large uncertainties). Again, the suspected binary nature of the primary (HD 74341 B) may be significantly biasing the derived satellite spot ratios.

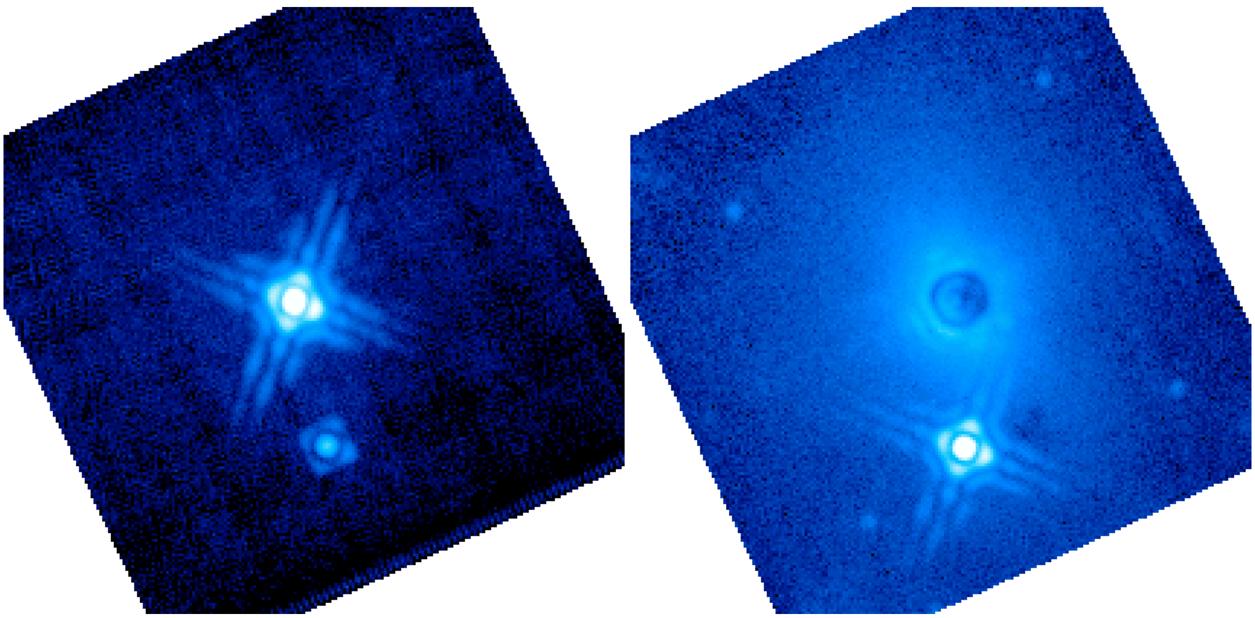

Figure 38: K1 observations of HD 74341 B obtained on 2018-03-25 after sky-subtraction.

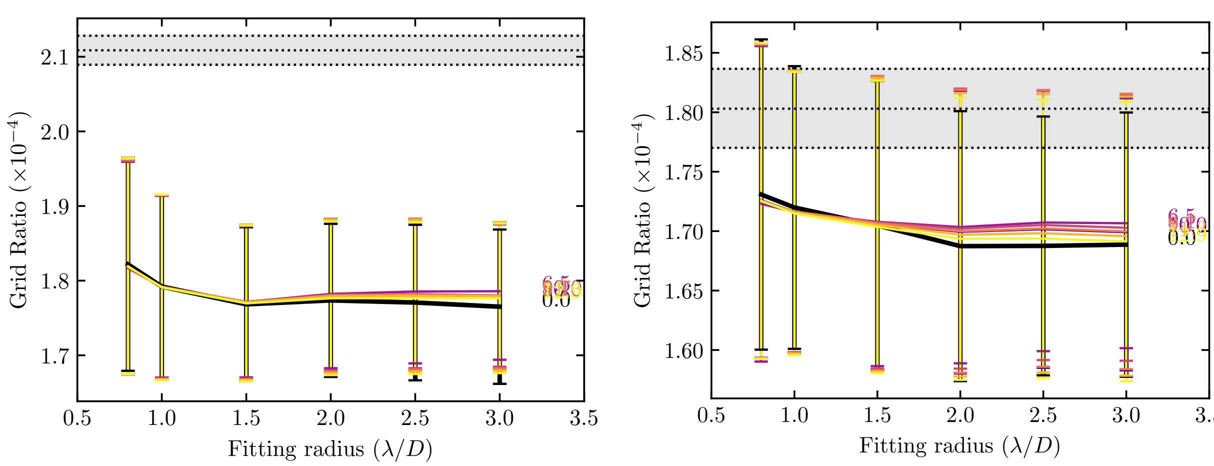

Figure 39: Satellite spot ratio derived from the HD 74341 B K1 dataset with the K1 (left) and H (right) apodizer as a plotted function of fitting radius. Adopted satellite spot ratios from Table 4 are show as grey shaded regions. While the derived ratio is consistent for the non-standard K1 filter/H apodizer instrument configuration, it is significantly discrepant for the K1 filter/K1 apodizer configuration.

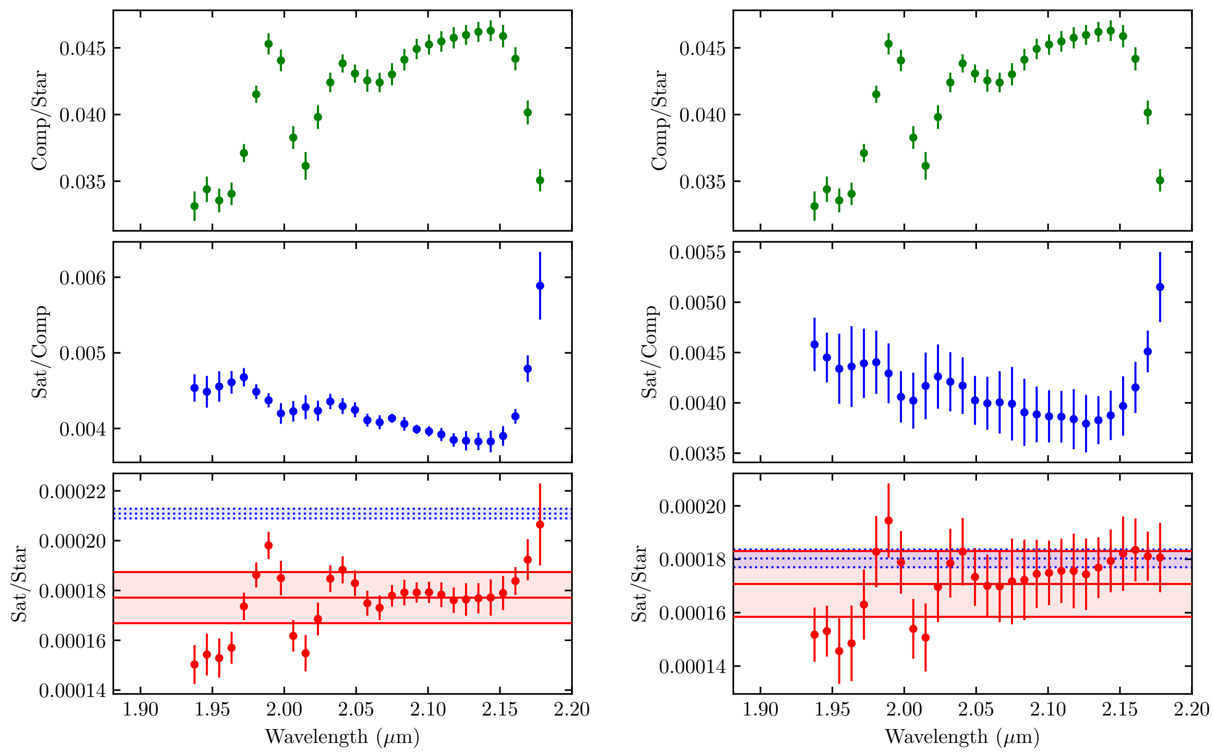

Figure 40: As Figure 30, but for the K1 filter/K1 apodizer (left) and K1 filter/H apodizer (right) data on HD 74341 B. The shorter-wavelength channels are affected both by water absorption in the Earth's atmosphere, leading to a significant drop in the S/N of the binary companion, and a poor wavelength solution (Figure 41). The adopted ratio is denoted by the blue shaded region for the K1 apodizer (left) and H apodizer (right).

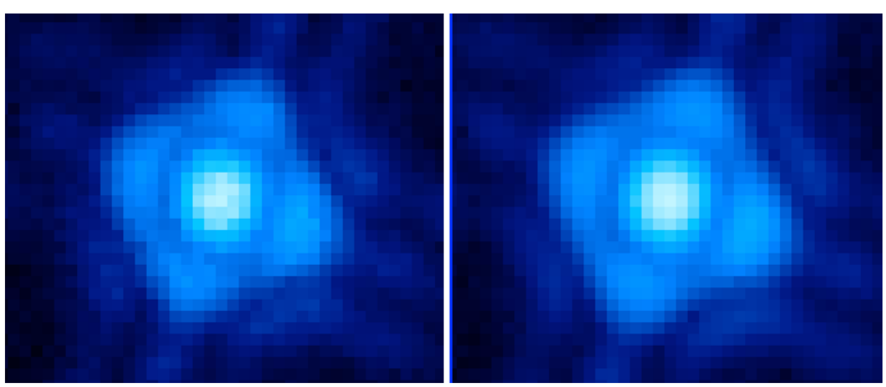

Figure 41: Comparison of GPI's PSF at 1.96 μm (left) and 2.05 μm (right) showing a significantly worse image reconstruction at shorter wavelengths.

The discrepancies seen between the data obtained with GPI's ASU and on-sky data may be caused by image motion in the unblocked images where both primary and secondary are visible, as the CAL loop is not providing tip/tilt correction to keep the star stable, or due to the rotation of the companion about the primary due to the change in parallactic angle over the course of the 60-90 second integration. While motion induced by uncorrected tip/tilt errors will affect both primary and secondary PSFs in the same way, parallactic rotation would only affect the PSF of the secondary. A visual inspection of the residual maps from the PSF fits did not reveal any evidence of elongation of the PSF of the secondary in the direction of parallactic rotation for any of the datasets, although there is evidence that HD 74341 B (the primary) is itself a tight binary that is barely resolved in the GPI images (H-band, Figure 42). The same elongation is seen in the K1 datasets, and a poor-quality J-band dataset obtained on 2018-03-09. If it is a barely-resolved binary, the satellite spot ratios derived from the H and K1 datasets on this target may be significantly biased, and not a good test of the adopted ratios in Table 4. No structure was seen in the residual maps for the HR 5625 and HD 215768 datasets, suggesting that the primaries in those systems are single.

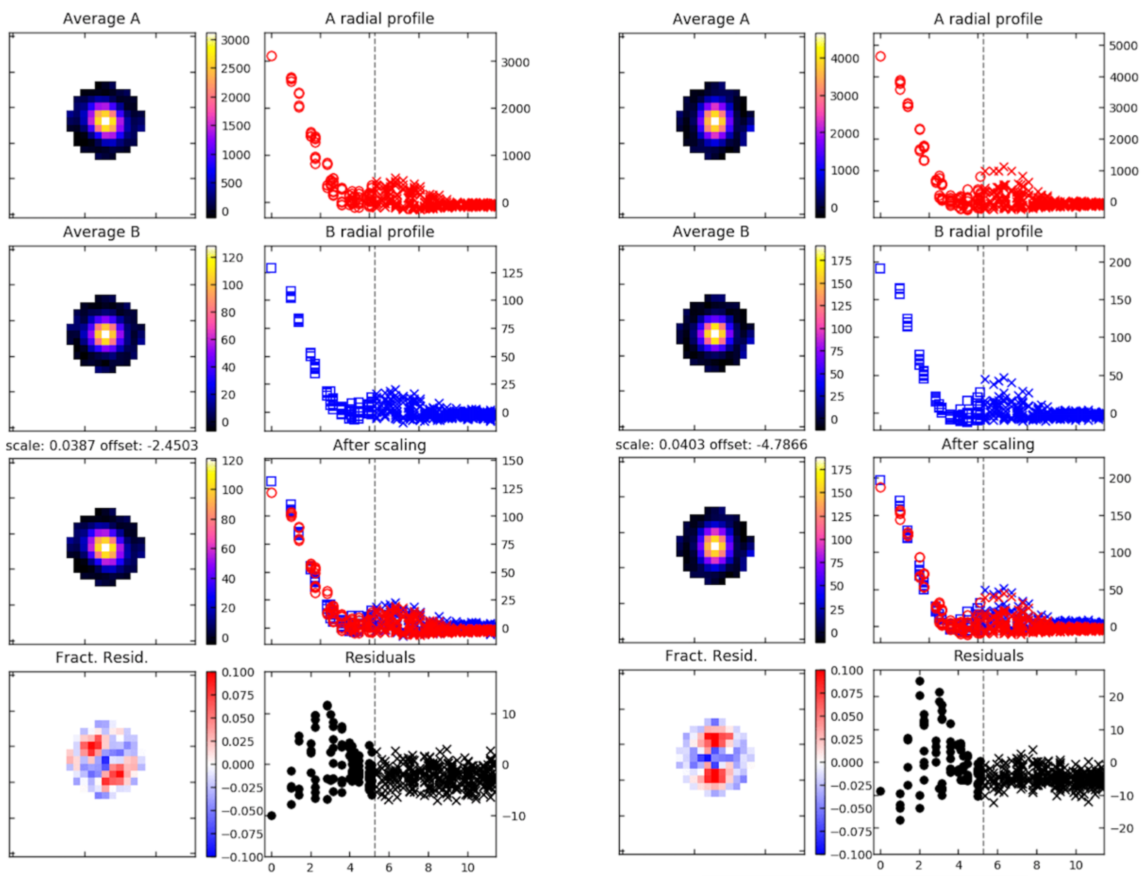

Figure 42: PSFs for the primary and secondary in the HD 74341 B system for the H-band dataset taken on 2018-03-08 (left) and 2018-03-26 (right). The residuals show a clear elongation of the primary (HD 74341 B). The axis of elongation differs by about 10 degrees in the 18-day baseline (the images here have not been de-rotated to put North up), consistent with the orbital motion expected for a pair of solar-mass stars with a semi-major axis of 1.5 au.

Table 6: Satellite spot ratios measured on-sky

Target	Filter	Apodizer	Order	Ratio (x10^{-4})	Δm	Note
HD 74341 B	J	J	1	1.33 ± 0.03	9.69 ± 0.03	
HD 74341 B	J	J	2	1.12 ± 0.07	9.88 ± 0.07	
HD 74341 B	J	H	1	1.84 ± 0.08	9.34 ± 0.05	
HD 74341 B	J	H	2	1.27 ± 0.04	9.74 ± 0.04	
HD 74341 B	H	H	1	1.79 ± 0.04	9.37 ± 0.03	
HD 74341 B	H	H	1	1.64 ± 0.03	9.46 ± 0.02	
HD 74341 B	H	H	1	1.52 ± 0.03	9.55 ± 0.02	with ND
HR 5625	H	H	1	2.36 ± 0.05†	9.07 ± 0.02	
HR 5625	H	H	1	2.34 ± 0.03†	9.08 ± 0.02	with ND
HD 215768	H	H	1	1.68 ± 0.05	9.44 ± 0.03	
HD 215768	H	H	1	1.83 ± 0.11	9.34 ± 0.06	
HD 74341 B	K1	K1	1	1.77 ± 0.10	9.38 ± 0.06	
HD 74341 B	K1	H	1	1.71 ± 0.12	9.42 ± 0.08	

† - Strong contamination from diffraction on two of the four satellite spots.